

Limits on non-canonical heating and turbulence in the intergalactic medium from the low redshift Lyman- α forest

James S. Bolton^{1*}, Prakash Gaikwad^{2,3}, Martin G. Haehnelt², Tae-Sun Kim⁴, Fahad Nasir⁵,
Ewald Puchwein⁶, Matteo Viel^{7,8,9,10} & Bart P. Wakker⁴

¹*School of Physics and Astronomy, University of Nottingham, University Park, Nottingham, NG7 2RD, UK*

²*Kavli Institute for Cosmology and Institute of Astronomy, Madingley Road, Cambridge, CB3 0HA, UK*

³*Max-Planck-Institut für Astronomie, Königstuhl 17, D-69117 Heidelberg, Germany*

⁴*Department of Astronomy, University of Wisconsin-Madison, 475 N. Charter St., Madison, WI 53706, USA*

⁵*Department of Physics and Astronomy, University of California, Riverside, CA 92521, USA*

⁶*Leibniz-Institut für Astrophysik Potsdam, An der Sternwarte 16, 14482 Potsdam, Germany*

⁷*SISSA - International School for Advanced Studies, Via Bonomea 265, I-34136 Trieste, Italy*

⁸*IFPU, Institute for Fundamental Physics of the Universe, Via Beirut 2, I-34151 Trieste, Italy*

⁹*INAF - Osservatorio Astronomico di Trieste, Via G.B. Tiepolo 11, I-34131 Trieste, Italy*

¹⁰*INFN - National Institute for Nuclear Physics, Via Valerio 2, I-34127 Trieste, Italy*

28 March 2022

ABSTRACT

We examine the column density distribution function (CDDF) and Doppler parameter distribution from hydrodynamical simulations and *Cosmic Origins Spectrograph* (COS) observations of the Ly α forest at redshift $0 \leq z \leq 0.2$. Allowing for a factor of two uncertainty in the metagalactic H I photoionisation rate, our hydrodynamical simulations are in good agreement ($1\text{--}1.5\sigma$) with the shape and amplitude of the observed CDDF at H I column densities $10^{13.3} \text{ cm}^{-2} \leq N_{\text{HI}} \leq 10^{14.5} \text{ cm}^{-2}$. However, the Doppler widths of the simulated lines remain too narrow with respect to the COS data. We argue that invoking AGN feedback does not resolve this discrepancy. We also disfavour enhanced photoheating rates as a potential solution, as this requires an unphysically hard UV background spectrum. If instead appealing to a non-canonical source of heating, an additional specific heat injection of $u \lesssim 6.9 \text{ eV m}_p^{-1}$ is required at $z \lesssim 2.5$ for gas that has $N_{\text{HI}} \simeq 10^{13.5} \text{ cm}^{-2}$ by $z = 0.1$. Alternatively, there may be an unresolved line of sight turbulent velocity component of $v_{\text{turb}} \lesssim 8.5 \text{ km s}^{-1} (N_{\text{HI}}/10^{13.5} \text{ cm}^{-2})^{0.21}$ for the coldest gas in the diffuse IGM.

Key words: methods: numerical - intergalactic medium - quasars: absorption lines

1 INTRODUCTION

Hydrodynamical simulations of the Ly α forest in a Λ CDM universe are in broad agreement with a range of observational data at redshift $2.5 \lesssim z \lesssim 4.5$ (Hernquist et al. 1996; Lukić et al. 2015; Bolton et al. 2017; Rossi 2020; Villaseñor et al. 2021). Allowing for the approximately factor of two uncertainty in the amplitude of the metagalactic UV background (e.g. Bolton et al. 2005; Becker & Bolton 2013), quantities such as the H I column density distribution (Altay et al. 2011; Rahmati et al. 2013), the Doppler widths of the Ly α absorption lines (Schaye et al. 2000; Hiss et al. 2018), and the distribution and power spectrum of the transmitted flux (Rorai et al. 2017; Walther et al. 2019) can be readily reproduced. While astrophysical processes such as feedback (Theuns et al. 2002b; Viel et al. 2013; Chabanier et al. 2020) and spatial fluctuations in the UV background (Greig et al. 2015; Upton Sanderbeck & Bird 2020; Molaro et al. 2022) can further modify this picture, these effects are typically of secondary importance to the assumed cosmological model and the

average photoionisation and photoheating rates (see McQuinn 2016, for a review).

Toward lower redshifts, however, the familiar character of the Ly α forest changes. Observationally, the redshifted Ly α transition shifts from optical to UV wavelengths at $z \simeq 1.5$, and can therefore only be observed from outside the atmosphere. Physically, the densities probed by the Ly α absorbers also change, from gas that is close to the mean background density, to higher density material that resides at the outskirts of galaxies (Theuns et al. 1998a; Davé et al. 1999, 2010; Nasir et al. 2017; Maitra et al. 2022). Recent progress has been largely driven by results from the *Cosmic Origins Spectrograph* (COS, Green et al. 2012) on the *Hubble Space Telescope* (e.g. Wakker et al. 2015; Danforth et al. 2016; Khaire et al. 2019; Kim et al. 2021). Intriguingly, the straightforward evolution of successful Ly α forest models at $z > 2$ to lower redshift does not automatically guarantee a good match to the Ly α forest absorption lines identified with COS. One challenge is correctly reproducing the incidence of Ly α forest absorbers at $z \sim 0$. Kollmeier et al. (2014) were the first to highlight a discrepancy between the observed and simulated H I column density distribution function (CDDF) at $z \sim 0$ for column densities $10^{13.6} \text{ cm}^{-2} \leq N_{\text{HI}} \leq 10^{14.4} \text{ cm}^{-2}$, finding the

* E-mail: james.bolton@nottingham.ac.uk

metagalactic H I photoionisation rate, Γ_{HI} , required by the observed CDDF was considerably larger (by factor of ~ 5) than predicted in the empirically calibrated [Haardt & Madau \(2012\)](#) UV background model. This implied that either the ionising photon production rate from galaxies and quasars had been significantly underestimated by [Haardt & Madau \(2012\)](#), or that the IGM simulations were missing an important physical ingredient. Subsequent work has revised this apparent discrepancy downward to a more manageable factor of two, either by using independent simulations ([Wakker et al. 2015](#); [Shull et al. 2015](#); [Gaikwad et al. 2017a](#); [Viel et al. 2017](#); [Nasir et al. 2017](#)), revising the predicted amplitude of the UV background in the empirical models ([Khaire & Srianand 2015, 2019](#); [Puchwein et al. 2019](#); [Faucher-Giguère 2020](#)), or by invoking black hole feedback that efficiently heats and ionises the low density IGM ([Christiansen et al. 2020](#)). Regardless of any remaining tension between data and theory, however, this work has demonstrated that the Ly α forest CDDF at $z \sim 0$ is a valuable diagnostic of ionising photon production and galactic feedback ([Gurvich et al. 2017](#)).

By contrast, the direct comparison of the Doppler parameter distribution of the Ly α forest absorption lines identified with COS to hydrodynamical simulations has received less attention. The few studies that have attempted this recently have (as for the CDDF) also struggled to reproduce the COS data at $0 \leq z \leq 0.2$, finding line widths that are too narrow compared to the observations ([Gaikwad et al. 2017b](#); [Viel et al. 2017](#); [Nasir et al. 2017](#)). The reason for this discrepancy remains unclear, but – assuming there are no unaccounted for instrumental systematics that systematically broaden the absorption lines – it suggests that the gas temperatures associated with the simulated Ly α absorbers may be too low and/or there is missing non-thermal broadening in the models. It is also not certain whether missing feedback can resolve this discrepancy. [Viel et al. \(2017\)](#) and [Nasir et al. \(2017\)](#) found that the AGN feedback model used in the Sherwood simulations ([Bolton et al. 2017](#)) has a very limited impact on the Ly α line widths; any additional hot gas was in the Warm-Hot IGM (WHIM), and was too highly ionised to detect in Ly α absorption. On the other hand, more recently [Christiansen et al. \(2020\)](#) have found that hot, highly ionised gas produced by the jet feedback model in the SIMBA simulation ([Davé et al. 2019](#)) significantly improves agreement with the mean Ly α forest transmission at $z < 0.5$. However, it is not obvious if this improved agreement also extends to the Doppler parameter distribution.

Hence, the goal of this work is to present a quantitative assessment of the additional heating and/or non-thermal contribution to the line widths required for consistency with the Ly α forest CDDF and Doppler parameter distribution from COS observations at $0 \leq z \leq 0.2$. We achieve this by forward modelling the COS data, and then fitting Voigt profiles to the simulations in the same manner as the observations. Our joint analysis of the CDDF and Doppler parameter distribution is then used to simultaneously constrain the metagalactic H I photoionisation rate and the effective power-law spectral shape of the UV background close to the Lyman limit. We shall argue that reproducing the Doppler widths of the Ly α absorbers in the COS data by boosting the thermal line widths requires a UV background with an unphysically hard ionising spectrum. This implies that there is still missing physics in the models, and that either an additional, non-canonical heating mechanism, or a source of non-thermal broadening that is missed by the simulations (e.g., IGM turbulence), is necessary for achieving consistency between hydrodynamical simulations of the Ly α forest and the COS data.

This paper is organised as follows. In Section 2 we describe the simulations used in this work. We then give an overview of the physical properties of simulated Ly α forest absorbers at $z \simeq 0.1$ in Sec-

tion 3, and perform an initial comparison of our simulated results to the COS data. Section 4 describes the relationship between the UV background spectral shape and the IGM temperature in our models, and outlines the simple model we use for including an unresolved turbulent contribution to the Ly α forest line widths. We then present and discuss our limits on non-canonical heating and/or the turbulent contribution required by the COS Ly α absorbers in Section 5, and summarise our conclusions in Section 6. The corrections to the simulated CDDF for box size and mass resolution that we use throughout this work are presented in Appendix A. An examination of the effect that noise and spectral resolution have on the CDDF and Doppler parameter distribution is presented in Appendix B, along with a test of our assumption that photoionisation equilibrium holds in the low redshift Ly α forest. In Appendix C, we compare the TNG100-1 simulation from the IllustrisTNG project ([Nelson et al. 2019](#)) to the COS data. We confirm that the Ly α forest line widths predicted by TNG100-1 are also narrower than observed at $z \simeq 0.1$.

Finally, throughout this work, it may be useful to recall that a $N_{\text{HI}} \sim 10^{13.5} \text{ cm}^{-2}$ Ly α forest absorber at $z = 0.1$ is typically associated with a gas overdensity of $\Delta \sim 10$ (or equivalently $n_{\text{H}} \sim 10^{-5.6} \text{ cm}^{-3}$) within our models. Comoving and proper distance units use the prefixes “c” and “p” respectively.

2 NUMERICAL MODELS

2.1 Hydrodynamical simulations

The 18 cosmological hydrodynamical simulations used in this work are listed in Table 1. The simulations were performed with a version of the Tree-PM SPH code P-GADGET-3 ([Springel 2005](#)), modified for the Sherwood simulation project ([Bolton et al. 2017](#); [Nasir et al. 2017](#)). Our fiducial box size is $L = 60h^{-1} \text{ cMpc}$ with 2×768^3 gas dark matter and gas particles, giving a gas (dark matter) particle mass of $M_{\text{gas}} = 6.38 \times 10^6 h^{-1} M_{\odot}$ ($M_{\text{dm}} = 3.44 \times 10^7 h^{-1} M_{\odot}$). This improves our fiducial mass resolution by a factor of 8 compared to [Nasir et al. \(2017\)](#). The gravitational softening length is set to 0.04 times the mean interparticle separation in all models. The cosmological parameters are $\Omega_{\text{m}} = 0.308$, $\Omega_{\Lambda} = 0.692$, $h = 0.678$, $\Omega_{\text{b}} = 0.0482$, $\sigma_8 = 0.829$ and $n = 0.961$ ([Planck Collaboration et al. 2014](#)), with a primordial helium fraction by mass of $Y_{\text{p}} = 0.24$ ([Hsyu et al. 2020](#)).

Our main simulation (AGN) incorporates energy-driven galactic outflows and AGN feedback using the model described in detail by [Puchwein & Springel \(2013\)](#). Briefly, the star formation model is based on [Springel & Hernquist \(2003\)](#), but for a [Chabrier \(2003\)](#) rather than [Salpeter \(1955\)](#) initial mass function and a galactic wind velocity that is directly proportional to the escape velocity of the galaxy. In the black hole feedback model, for the “quasar” mode when accretion rates are above 0.01 of the Eddington rate, 0.5 per cent of the accreted rest mass energy is thermally coupled to the gas. For lower accretion rates the “radio” mode is used instead. This is triggered for a fractional increase in the black hole mass of 10^{-4} , with 2 per cent of the rest mass energy used for injecting hot AGN bubbles. This is the same star formation and AGN feedback model used in our earlier work on the Ly α forest at $z \simeq 0.1$ ([Viel et al. 2017](#); [Nasir et al. 2017](#)).

To explore the effect of AGN feedback further, we also now consider a second model (StrongAGN) where the fractional increase in the black hole mass required for triggering the radio mode is increased to 10^{-2} , with 8 per cent of the rest mass energy now used to inject hot AGN bubbles. This is the same as the “stronger radio”

model used by [Henden et al. \(2018\)](#), and it leads to less frequent but more energetic bubble injections and substantially lower gas fractions in the vicinity of haloes. We use this to provide a model that predicts a gas mass in the Warm-Hot IGM (WHIM) at low redshift that mimics the effect of jet-mode heating in the SIMBA simulation used by [Christiansen et al. \(2020\)](#) (see Section 3.1 for further details).

For the remainder of the simulations in Table 1 we ignore star formation and feedback, and instead directly convert gas with temperature $T < 10^5$ K and density $\Delta = \rho/\langle\rho\rangle > 10^3$ into collisionless particles ([Viel et al. 2004](#)). This “Quick-Ly α ” approach has been shown to be a reasonable approximation for unsaturated absorption lines, $N_{\text{HI}} < 10^{14.5} \text{ cm}^{-2}$, in the low redshift Ly α forest ([Nasir et al. 2017](#)). Importantly, the Quick-Ly α approach is less computationally expensive than the AGN feedback model, and for this reason we use it to create a grid of 11 simulations (H00–H10) with different IGM thermal histories that we use to obtain our UV background constraints in Section 5.

Photoionisation and heating by a spatially uniform UV background is included in all simulations assuming ionisation equilibrium. We use the equilibrium equivalent rates from the UV background model of [Puchwein et al. \(2019, hereafter P19\)](#). This has the advantage of correctly incorporating non-equilibrium ionisation effects on the ionised fraction and gas temperature, but without the additional computational overhead of solving a non-equilibrium thermo-chemistry network. At $z = 0.1$, the P19 model has a photoionisation rate $\log(\Gamma_{\text{HI}}^{\text{P19}}/\text{s}^{-1}) = -13.04$ and predicts a gas temperature at the mean density of $T_0 \simeq 4200$ K, and a power-law temperature-density relation, $T = T_0 \Delta^\gamma$, where $\gamma \simeq 1.58$ for $\Delta = \rho/\langle\rho\rangle \lesssim 10$. In the 11 Quick-Ly α simulations (H00–H10) we have varied the UV background photoheating rates, ε_i , in the P19 UV background model. We scale the hydrogen and helium photoheating rates by a constant ζ , where $\varepsilon_i = \zeta \varepsilon_i^{\text{P19}}$ and $i = \text{HI}, \text{HeI}, \text{HeII}$ (cf. [Becker et al. 2011](#)). Self-shielding of dense gas to ionising photons is included on-the-fly in all simulations following [Rahmati et al. \(2013\)](#). Metal line cooling is not included, although [Tepper-García et al. \(2012\)](#) found this should have a very small effect on the column densities and Doppler parameters of low redshift Ly α forest absorbers (see their fig. C2). We also indirectly test this in Appendix C by performing a Voigt profile analysis on Ly α forest spectra drawn from the Illustris TNG100-1 simulation, which does include metal line cooling.

For comparison with the canonical UV photoheating paradigm, following [Kollmeier et al. \(2014\)](#) we also consider an alternative model (Blazar) where heating in the IGM at $z < 3$ is dominated by TeV emission from blazars. This results in a much higher temperature in the low-density IGM, $T_0 \simeq 31\,100$ K, compared to UV photoheating models, with a temperature-density relation that is “inverted” (i.e. $\gamma < 1$) due to a volumetric heating rate that is independent of density ([Chang et al. 2012](#)). We adopt the intermediate heating model from [Puchwein et al. \(2012\)](#) for this purpose (see their eq. (1) and table 1), and perform the simulation using the Quick-Ly α approximation.

Finally, we perform four more Quick-Ly α simulations to assess the convergence of our results with box size and mass resolution; these models are listed in the lower section of Table 1. We use these models to apply a correction to the simulated CDDF at our fiducial mass resolution and box size. This correction is listed in Table A1 in Appendix A, along with a more detailed discussion of the convergence properties of the Quick-Ly α simulations.

2.2 Simulated and observed Ly α forest spectra

Simulated Ly α forest spectra are extracted using an approach similar to [Nasir et al. \(2017\)](#). We randomly draw 16384 lines of sight parallel to the box axes, where each line of sight has 2048 pixels. The Ly α optical depths are then obtained from the particle data using the interpolation scheme described by [Theuns et al. \(1998b\)](#) combined with the Voigt profile approximation from [Tepper-García \(2006\)](#).

In this work we will compare the simulated spectra to observational measurements of the Ly α forest CDDF and Doppler parameter distribution first described in [Viel et al. \(2017\)](#). These data are obtained from 44 AGN spectra, selected to have a signal-to-noise per resolution element of $S/N > 20$ and an emission redshift of $0.1 < z_{\text{em}} < 0.35$, and form part of the larger data set recently presented by [Kim et al. \(2021\)](#). Further details regarding the COS data reduction and Voigt profile fitting can be found in [Wakker et al. \(2015\)](#) and [Kim et al. \(2021\)](#). The Voigt profile fits to the COS data and simulations have been obtained using the Ly α transition only. The line list we use consists of 704 H I Ly α lines with mean redshift $\langle z \rangle = 0.09$, mean column density $\langle \log(N_{\text{HI}}/\text{cm}^{-2}) \rangle = 13.29$ and mean Doppler parameter $\langle b \rangle = 36.6 \text{ km s}^{-1}$. The total redshift path length of the data is $\Delta z = 4.991$, covering the Ly α forest at $0 \leq z \leq 0.2$. As already shown in [Nasir et al. \(2017\)](#), the CDDF and Doppler parameter distribution we use are consistent with independent measurements using COS data from [Danforth et al. \(2016\)](#) and [Gaikwad et al. \(2017b\)](#) over the range of interest for this work.

In order to approximately forward model the COS data, all the simulated spectra are convolved with the COS line spread function¹ at 1341 Å, for central wavelength G130M/1327 at lifetime position LP1. The spectra are then rebinned onto pixels of width 0.02991 Å (i.e 3 times the COS binning of 0.00997 Å following [Kim et al. \(2021\)](#)) and Gaussian distributed noise with a flux independent signal-to-noise ratio of $S/N = 30$ per 19 km s^{-1} resolution element (i.e. $S/N \sim 17.7$ per pixel) is added. Voigt profile fitting to the simulated Ly α spectra is then performed with VPFIT version 10 ([Carswell & Webb 2014](#)), which deconvolves the (already convolved) mock spectra with the instrument profile to obtain the intrinsic line widths. We emphasise that, to ensure a fair comparison between observations and simulations, we have considered *only* the Ly α lines obtained with VPFIT in this work. This minimises any biases that would arise if, e.g., we had used higher order Lyman series information to perform a curve-of-growth analysis on either the observational or simulated data alone.

We assess the role that a different signal-to-noise ratio or line spread function may have on the recovery of the CDDF and Doppler parameter distribution in Appendix B. To summarise those results, we find that absorption lines with $10^{13.3} \text{ cm}^{-2} \leq N_{\text{HI}} \leq 10^{14.5} \text{ cm}^{-2}$ and $20 \text{ km s}^{-1} \leq b \leq 90 \text{ km s}^{-1}$ will remain insensitive to the expected variations in the S/N or line spread function. We will only use the absorption lines in these ranges when obtaining UV background constraints from the COS data. This sub-set consists of 297 H I Ly α lines with mean redshift $\langle z \rangle = 0.09$, mean column density $\langle \log(N_{\text{HI}}/\text{cm}^{-2}) \rangle = 13.70$ and mean Doppler parameter $\langle b \rangle = 39.9 \text{ km s}^{-1}$.

¹ <https://www.stsci.edu/hst/instrumentation/cos/performance/spectral-resolution>

Table 1. Summary of the P-GADGET-3 simulations used in this work. From left to right, the columns list the simulation name, the box size in $h^{-1}\text{cMpc}$, the gas particle mass in $h^{-1}M_{\odot}$, the factor, ζ , by which the equilibrium equivalent photoheating rates from Puchwein et al. (2019) are increased for each model, the gas temperature, T_0 , at the mean density at $z = 0.1$, the slope, $\gamma - 1$, of the power-law temperature-density relation at $z = 0.1$, the effective power-law spectral index, α_{eff} , for the UV background at $z = 0.1$ (see Section 4.1 for details), the mean transmission of the Ly α forest at $z = 0.1$ assuming the Puchwein et al. (2019) photoionisation rate $\log(\Gamma_{\text{HI}}^{\text{P19}}/\text{s}^{-1}) = -13.04$, the photoionisation rate, $\Gamma_{\text{HI}}^{\text{CDDF}}$, required to match the amplitude of the CDDF at $z = 0.1$, the ratio of this quantity to the Puchwein et al. (2019) value, and the ratio to the Haardt & Madau (2012) value, $\log(\Gamma_{\text{HI}}^{\text{HM12}}/\text{s}^{-1}) = -13.45$. The upper section of the table lists the simulations used to test the effect of AGN feedback (Puchwein & Springel 2013) and blazar heating (Puchwein et al. 2012) on the Ly α forest absorption lines. The Quick-Ly α simulations that form our thermal history grid are listed in the middle section of the table. The lower section of the table lists the Quick-Ly α simulations used to test the effect of simulation box size and mass resolution in Appendix A.

Model	L_{box} [$h^{-1}\text{cMpc}$]	N_{part}	M_{gas} [$h^{-1}M_{\odot}$]	ζ	T_0 [K]	$\gamma - 1$	α_{eff}	$\langle F \rangle$	$\log(\frac{\Gamma_{\text{HI}}^{\text{CDDF}}}{\text{s}^{-1}})$	$\frac{\Gamma_{\text{HI}}^{\text{CDDF}}}{\Gamma_{\text{HI}}^{\text{P19}}}$	$\frac{\Gamma_{\text{HI}}^{\text{CDDF}}}{\Gamma_{\text{HI}}^{\text{HM12}}}$
AGN	60.0	2×768^3	6.38×10^6	1.00	4216	0.58	1.17	0.981	-13.22	0.66	1.69
StrongAGN	60.0	2×768^3	6.38×10^6	1.00	4274	0.59	1.17	0.988	-13.50	0.35	0.90
Blazar	60.0	2×768^3	6.38×10^6	1.00	31069	-0.85	–	0.989	-13.41	0.43	1.11
H00	60.0	2×768^3	6.38×10^6	0.65	3262	0.58	2.89	0.981	-13.22	0.67	1.71
H01	60.0	2×768^3	6.38×10^6	0.82	3703	0.58	1.86	0.982	-13.22	0.66	1.70
H02	60.0	2×768^3	6.38×10^6	1.00	4174	0.58	1.17	0.983	-13.22	0.67	1.73
H03	60.0	2×768^3	6.38×10^6	1.20	4743	0.59	0.65	0.983	-13.22	0.67	1.73
H04	60.0	2×768^3	6.38×10^6	1.42	5129	0.58	0.24	0.984	-13.24	0.64	1.64
H05	60.0	2×768^3	6.38×10^6	1.65	5713	0.58	-0.07	0.985	-13.27	0.59	1.51
H06	60.0	2×768^3	6.38×10^6	1.90	6194	0.59	-0.33	0.985	-13.28	0.58	1.49
H07	60.0	2×768^3	6.38×10^6	2.16	6680	0.59	-0.54	0.986	-13.31	0.54	1.38
H08	60.0	2×768^3	6.38×10^6	2.72	7797	0.59	-0.86	0.987	-13.35	0.49	1.25
H09	60.0	2×768^3	6.38×10^6	3.33	8778	0.59	-1.09	0.987	-13.40	0.44	1.13
H10	60.0	2×768^3	6.38×10^6	4.70	10817	0.59	-1.41	0.989	-13.47	0.38	0.97
L40	40.0	2×512^3	6.38×10^6	1.00	4148	0.58	1.17	0.983	-13.25	0.62	1.59
L80	80.0	2×1024^3	6.38×10^6	1.00	4182	0.58	1.17	0.984	-13.26	0.60	1.55
N512	60.0	2×512^3	2.15×10^7	1.00	4473	0.59	1.17	0.982	-13.20	0.70	1.80
N1024	60.0	2×1024^3	2.69×10^6	1.00	4127	0.59	1.17	0.983	-13.24	0.64	1.63

3 THE CDDF AND DOPPLER PARAMETER DISTRIBUTION

3.1 Physical properties of unsaturated Ly α forest absorbers at $z=0.1$

First, it is instructive to briefly recap the general properties of the low redshift Ly α forest predicted in cosmological hydrodynamical simulations. In Fig. 1 we show a $60h^{-1}\text{cMpc} \times 60h^{-1}\text{cMpc}$ slice through the AGN simulation volume, displaying the gas density at $z = 0.1$ projected over a distance of $500h^{-1}\text{ckpc}$. The Ly α absorbers with HI column densities $10^{13.3}\text{cm}^{-2} \leq N_{\text{HI}} \leq 10^{14.5}\text{cm}^{-2}$ in the slice are over-plotted as coloured circles. Rather than fit Voigt profiles – as we do in the rest of this work – following Gurvich et al. (2017), these HI column densities are obtained by integrating the HI number densities in the model over a scale of 50km s^{-1} . The cyan stars show the position of haloes with total mass $M_{\text{h}} \geq 10^{12}M_{\odot}$.

On visual inspection of Fig. 1, we observe the Ly α forest absorbers are located in the overdense filaments and nodes in the web-like distribution of intergalactic gas (see also Tonnesen et al. 2017). This is quantified further in the right panel of Fig. 1, which shows the fraction of these absorbers within 1, 2 or 3 virial radii² of haloes with masses $10^{10}M_{\odot} \leq M_{\text{h}} < 10^{12}M_{\odot}$ (upper panel) and $M_{\text{h}} \geq 10^{12}M_{\odot}$ (lower panel). We find that only a few per cent of Ly α forest ab-

sorbers with $N_{\text{HI}} \leq 10^{14}\text{cm}^{-2}$ are within $r < R_{\text{vir}}$, with a fraction that increases with N_{HI} for halo masses $10^{10}M_{\odot} \leq M_{\text{h}} < 10^{12}M_{\odot}$.

For comparison, using the CGM² (Cosmic Origins Spectrograph and Gemini Mapping the Circumgalactic Medium) survey, Wilde et al. (2021) have recently found that – while HI absorption lines with $N_{\text{HI}} < 10^{14}\text{cm}^{-2}$ are not strongly associated with massive galaxies – absorbers with $N_{\text{HI}} > 10^{14}\text{cm}^{-2}$ have a high probability (i.e. > 50 per cent) of residing within $1.2R_{\text{vir}}$ ($2.4R_{\text{vir}}$) of galaxies with stellar masses $10^{9.2}M_{\odot} < M_{\star} < 10^{9.9}M_{\odot}$ ($M_{\star} > 10^{9.9}M_{\odot}$). As a rough comparison, for halo masses $10^{10}M_{\odot} \leq M_{\text{h}} < 10^{12}M_{\odot}$, we find the fraction of HI absorbers within $r < 3R_{\text{vir}}$ in our simulations increases with N_{HI} , from ~ 20 per cent at $\log(N_{\text{HI}}/\text{cm}^{-2}) = 13.4 \pm 0.1$ up to almost 60 per cent at $\log(N_{\text{HI}}/\text{cm}^{-2}) = 14.4 \pm 0.1$. The qualitative picture is therefore one where the majority of the strongest absorbers with $N_{\text{HI}} > 10^{14}\text{cm}^{-2}$ occur close to haloes, while the majority of weaker absorbers are associated with intergalactic gas and are at $r > 3R_{\text{vir}}$ (see also Chen & Mulchaey 2009; Tejos et al. 2014; Keeney et al. 2018). In total, 29.2 (1.5) per cent of the identified HI absorbers with $10^{13.3}\text{cm}^{-2} \leq N_{\text{HI}} \leq 10^{14.5}\text{cm}^{-2}$ are within $3R_{\text{vir}}$ (R_{vir}) of a halo with $10^{10}M_{\odot} \leq M_{\text{h}} < 10^{12}M_{\odot}$.

By contrast, for the more massive haloes with $M_{\text{h}} \geq 10^{12}M_{\odot}$ shown in the lower right panel of Fig. 1, only 11.7 (1.4) per cent of identified HI absorbers with $10^{13.3}\text{cm}^{-2} \leq N_{\text{HI}} \leq 10^{14.5}\text{cm}^{-2}$ are within $r < 3R_{\text{vir}}$ ($r < R_{\text{vir}}$) of a halo. Interestingly, the fraction of gas with $r < 3R_{\text{vir}}$ now has the opposite trend with N_{HI} for the most massive haloes, where there are now relatively fewer absorbers in the vicinity of haloes as N_{HI} increases. This is due to the presence of hot, collisionally ionised gas around the more massive haloes, associated with shocks from gravitational infall and AGN feedback.

² In this work we identify the virial radius, R_{vir} , as the radius of a sphere centred at the halo centre of mass that has mean density Δ_c times the critical density, where Δ_c is given by eq. (6) of Bryan & Norman (1998).

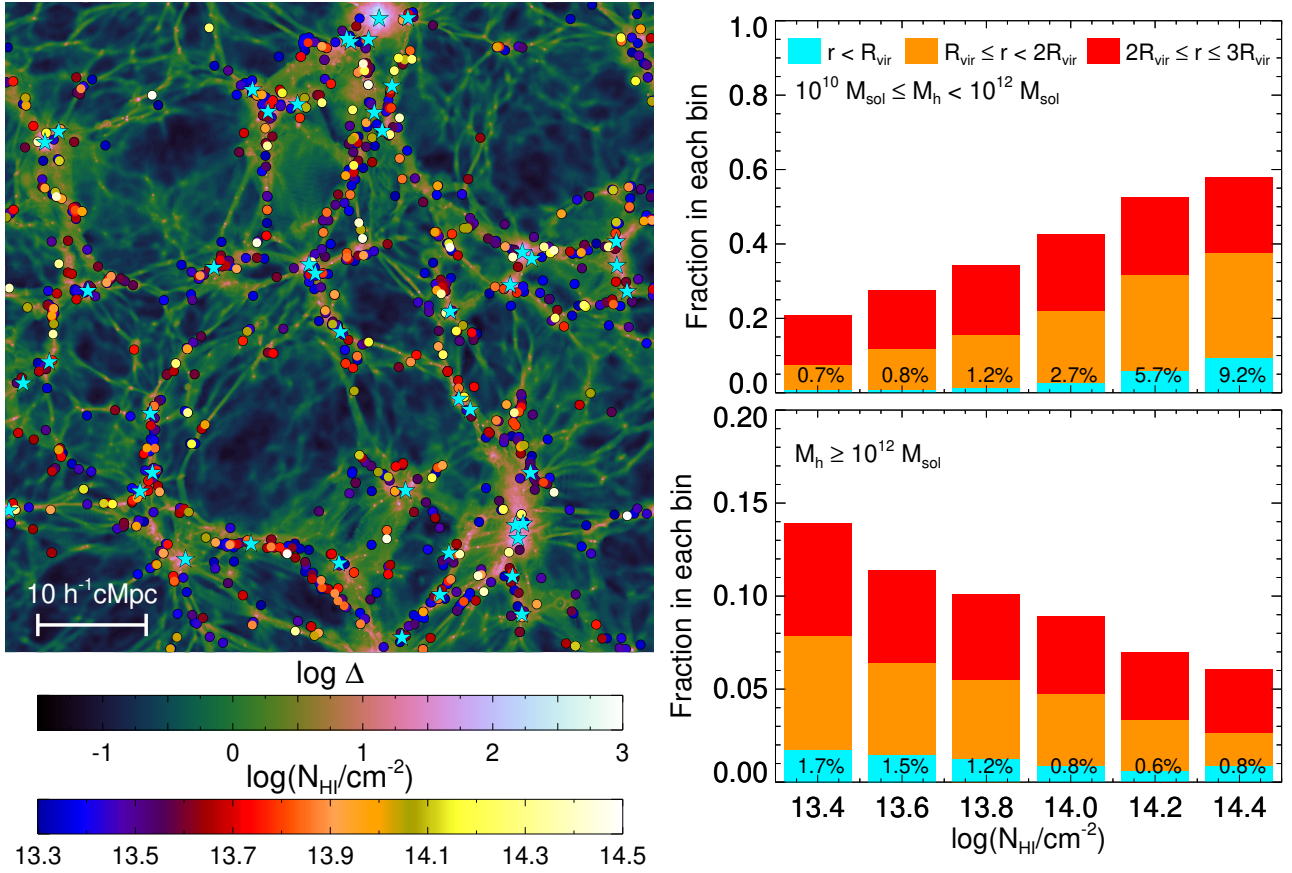


Figure 1. *Left:* A square slice ($60h^{-1}\text{cMpc}$ on each side) displaying the logarithm of the gas density, $\log \Delta = \log(\rho/\langle\rho\rangle)$, in the AGN simulation at $z = 0.1$, projected over a distance of $500h^{-1}\text{ckpc}$. The Ly α absorbers in the slice with H I column densities $10^{13.3}\text{cm}^{-2} \leq N_{\text{HI}} \leq 10^{14.5}\text{cm}^{-2}$ are over-plotted as coloured circles. The cyan stars show the location of haloes in the slice with total mass $M_{\text{h}} \geq 10^{12}M_{\odot}$. *Right:* The fraction of Ly α absorbers in the full simulation volume at redshift $z = 0.1$, in bins of width $\Delta \log(N_{\text{HI}}/\text{cm}^{-2}) = 0.2$, located within one (cyan bars), two (orange bars) or three (red bars) virial radii, R_{vir} , of haloes with total mass $10^{10}M_{\odot} \leq M_{\text{h}} < 10^{12}M_{\odot}$ (upper panel) or $M_{\text{h}} \geq 10^{12}M_{\odot}$ (lower panel). Note the different scale on the vertical axis of the lower panel. The percentages at the base of each bar give the fraction of absorbers within $r < R_{\text{vir}}$.

Table 2. The percentage of Ly α absorbers with $20\text{km s}^{-1} \leq b \leq 90\text{km s}^{-1}$ and $10^{13.3}\text{cm}^{-2} \leq N_{\text{HI}} \leq 10^{14.5}\text{cm}^{-2}$ in the AGN, StrongAGN, H02 and Blazar simulations that are associated with the four temperature-density phases defined by Davé et al. (2010). For comparison, the number in parentheses gives the baryon mass fraction associated with each phase, where we also include stars in the condensed phase. The mass fraction in the condensed+stars phase is artificially high in the H02 and Blazar models as a result of using the Quick-Ly α scheme for converting gas to star particles. Note also that while the relative fraction of Ly α absorbers in each phase remains similar across all models, the mass fraction in the WHIM (shown in parentheses) increases significantly in the StrongAGN simulation.

Model	Diffuse IGM	WHIM	Hot halo	Condensed(+stars)
	$T < 10^5\text{K}, \Delta < 97.2$	$T \geq 10^5\text{K}, \Delta < 97.2$	$T \geq 10^5\text{K}, \Delta \geq 97.2$	$T < 10^5\text{K}, \Delta \geq 97.2$
AGN	83.4 (36.7)	15.2 (37.9)	0.7 (16.1)	0.7 (9.3)
StrongAGN	82.1 (20.1)	16.8 (68.4)	0.6 (3.0)	0.5 (8.5)
H02 (No SF/feedback)	87.3 (35.5)	10.2 (21.2)	2.0 (13.9)	0.5 (29.4)
Blazar (No SF/feedback)	82.9 (23.2)	14.9 (34.3)	1.9 (13.5)	0.3 (29.0)

The physical properties of the Ly α forest absorbers are explored further in Fig. 2, where the Doppler parameters, b , and H I column densities, N_{HI} , obtained from fitting mock spectra with Voigt profiles are displayed in the b - N_{HI} plane. In each panel, the colour scale shows the (optical depth weighted) gas density, gas temperature, baryon phase, and the ratio b/b_{therm} (where $b_{\text{therm}} = (2k_{\text{B}}T/m_{\text{H}})^{1/2}$ is the thermal line width) associated with the absorbers. The baryon phase definitions follow those introduced by Davé et al. (2010) (see Table 2 for details). The absorption lines enclosed by the dashed

lines (i.e. for $10^{13.3}\text{cm}^{-2} \leq N_{\text{HI}} \leq 10^{14.5}\text{cm}^{-2}$, $20\text{km s}^{-1} \leq b \leq 90\text{km s}^{-1}$) are associated with predominantly photoionised gas with a median gas density $\log \Delta = 1.14$, median temperature $T = 38380\text{K}$ and median $b/b_{\text{therm}} = 1.28$. Note that b/b_{therm} is consistent with curve-of-growth analyses that use higher order Lyman series lines to separate unresolved Ly α components. For example, Danforth et al. (2010) perform a curve-of-growth analysis on 164 Ly α absorbers using HST/STIS data, finding a median ratio $b_{\text{Ly}\alpha}/b_{\text{cog}} = 1.26^{+0.49}_{-0.25}$ (see also Shull et al. 2000; Danforth & Shull 2008). In general, the

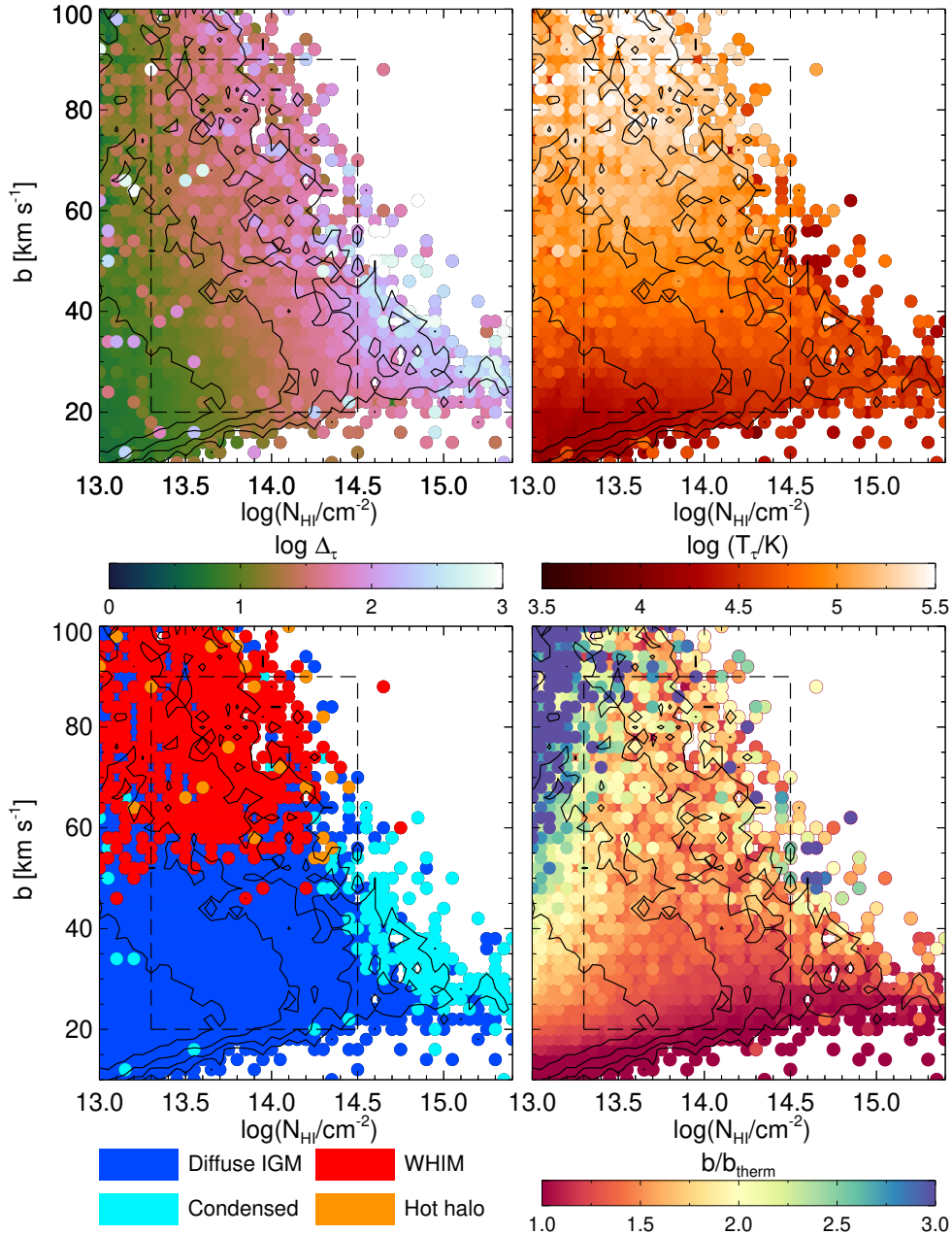


Figure 2. *Upper left:* The Doppler parameter, b , against the logarithm of the H I column density, $\log N_{\text{HI}}$, for Ly α absorption lines at redshift $z = 0.1$ in the AGN simulation. The number of absorption lines increases by 0.5 dex within each contour, where the colour indicates the logarithm of the optical depth weighted gas density, $\log \Delta_{\tau}$, associated with each absorber. The boxed region corresponds to the column densities and Doppler parameters used to constrain the UV background in this work; these represent 28 per cent of all the identified lines. *Upper right:* As for the upper left panel, except the colour now indicates the logarithm of the optical depth weighted gas temperature for each absorber. *Lower left:* As for the upper left panel, except the four colours now indicate the baryon phase associated with the absorbers, following [Davé et al. \(2010\)](#). The phases are: diffuse IGM ($T < 10^5$ K, $\Delta < 97.2$), WHIM ($T \geq 10^5$ K, $\Delta < 97.2$), hot halo ($T \geq 10^5$ K, $\Delta \geq 97.2$) and condensed ($T < 10^5$ K, $\Delta \geq 97.2$). The fraction of absorbers in the boxed region within each phase are: 83 per cent diffuse IGM, 15 per cent WHIM, 1 per cent hot halo and 1 per cent condensed (see also Table 2). *Lower right:* As for the upper left panel, except now showing the ratio of the Doppler parameters to the expected thermal line widths, b/b_{therm} , where $b_{\text{therm}} = (2k_{\text{B}}T_{\tau}/m_{\text{H}})^{1/2}$.

larger column densities and Doppler parameters are associated with higher gas densities and temperatures, respectively. The majority of the absorbers (90 per cent) with $10^{13.3} \text{ cm}^{-2} \leq N_{\text{HI}} \leq 10^{14.5} \text{ cm}^{-2}$ exhibit suprathermal line widths and 83 per cent are associated with the diffuse IGM. Only the absorbers close to the lower boundary of the b - N_{HI} plane have thermal widths; most of the other Ly α lines are also broadened by peculiar motions and the blending of unre-

solved Ly α components, gas pressure (Jeans) smoothing and expansion with the Hubble flow.

Finally, in Table 2 we summarise the percentage of Ly α absorbers associated with the four gas phases (diffuse IGM, WHIM, hot halo, and condensed) defined by [Davé et al. \(2010\)](#) are listed for the AGN, StrongAGN, H02 (i.e. the Quick-Ly α simulation with no feedback or star formation) and Blazar models. Note that a similar fraction of

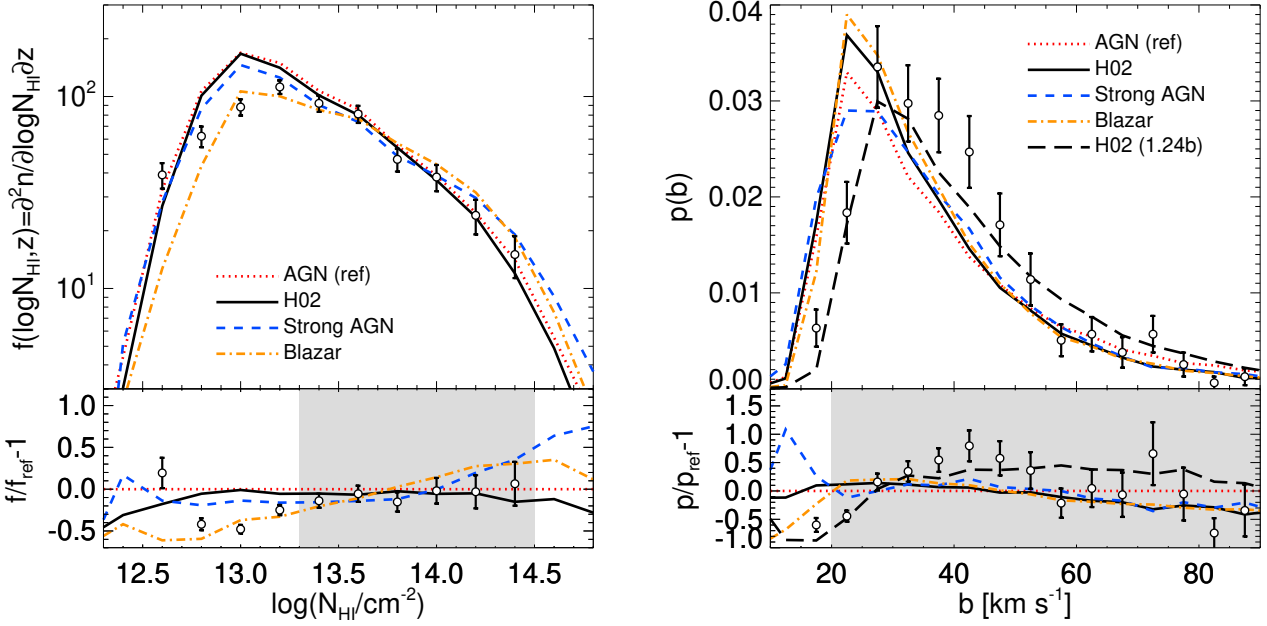


Figure 3. *Left:* The column density distribution function (CDDF) measured from COS data (open circles, Viel et al. 2017) for Ly α absorbers with Doppler parameters $20 \text{ km s}^{-1} \leq b \leq 90 \text{ km s}^{-1}$, compared to the CDDF obtained from the AGN (red dotted curve), StrongAGN (blue dashed curve), Blazar (orange dot-dashed curve) and H02 (black solid curve) models. Note the CDDF is incomplete at $N_{\text{HI}} \lesssim 10^{13.3} \text{ cm}^{-2}$. Following Viel et al. (2017), the column densities obtained from the mock spectra have been linearly rescaled to achieve good agreement with the observed CDDF. A correction for box size and mass resolution has also been applied to the simulations (see Appendix A for details). The lower panel displays the residuals with respect to the AGN model. *Right:* The corresponding Doppler parameter probability distribution for Ly α absorbers with column densities $10^{13.3} \text{ cm}^{-2} \leq N_{\text{HI}} \leq 10^{14.5} \text{ cm}^{-2}$. The simulated line widths are narrower than the observational measurements. The black dashed curve shows the H02 simulation after the Doppler widths have been increased by a factor of 1.24. The grey shading in the lower panels display the N_{HI} and b range where we judge the comparison between observations and simulations to be reliable (see Appendix B for details).

the Ly α absorbers are associated with each baryon phase in all four simulations. This may be contrasted with the baryon mass fraction in each phase, shown in the parentheses in Table 2. In particular, the mass fraction associated with the WHIM increases dramatically in the StrongAGN model. However, this has a very limited effect on the fraction of *absorbers* in each phase, since most of this gas is too hot and/or low density to produce Ly α absorption lines (Viel et al. 2017).

3.2 Comparison of the models to COS data

We now perform an initial comparison of the simulated spectra to measurements of the column density distribution function (CDDF) and Doppler parameter distribution. The CDDF and Doppler parameter distribution observations were first presented in Viel et al. (2017). In this work, the 1σ uncertainties on the measurements are obtained using 10^3 bootstrap samples with replacement.

The AGN, StrongAGN, Blazar and H02 simulations are compared directly to the COS data in Fig. 3. Following Viel et al. (2017), the HI column densities from each model have been rescaled by a constant to match the amplitude of the observed CDDF at $10^{13.3} \text{ cm}^{-2} \leq N_{\text{HI}} \leq 10^{14.5} \text{ cm}^{-2}$. Assuming the Ly α absorbers are in photoionisation equilibrium, this is equivalent to a rescaling of the HI photoionisation rate Γ_{HI} , since $N_{\text{HI}} \propto \Gamma_{\text{HI}}^{-1}$. We verify in Appendix B that this approximation is a good one for modelling the CDDF at $10^{13.3} \text{ cm}^{-2} \leq N_{\text{HI}} \leq 10^{14.5} \text{ cm}^{-2}$ (although see also Khaire et al. (2019), who find this is not the case for the Ly α forest power spectrum at $z < 0.5$. We speculate this may be due to including absorbers with $N_{\text{HI}} > 10^{14.5} \text{ cm}^{-2}$, and/or the influence of hot

gas that produces absorption near the continuum that is too weak and/or broad to be identified reliably with VPFIT). The photoionisation rate required to match the observed CDDF³, $\Gamma_{\text{HI}}^{\text{CDDF}}$, is a factor of 0.4–0.6 times the P19 UV background model value at $z = 0.1$, suggesting that the P19 model may overproduce the UV background at $z \sim 0.1$. The simulations with a higher fraction of hot gas, either from additional physics (StrongAGN and Blazar) or from artificially increased photoheating rates (e.g. H10) require the smallest $\Gamma_{\text{HI}}^{\text{CDDF}}$ as a result of the reduced recombination rate in the hotter IGM (see the second last column of Table 1).

For comparison to the literature, we also calculate the ratio of $\Gamma_{\text{HI}}^{\text{CDDF}}$ to the photoionisation rate at $z = 0.1$ from the Haardt & Madau (2012, hereafter HM12) UV background model; we list this in the final column of Table 1. For absorbers with $10^{13.6} \text{ cm}^{-2} \leq N_{\text{HI}} \leq 10^{14.4} \text{ cm}^{-2}$, Kollmeier et al. (2014) found that $\Gamma_{\text{HI}}^{\text{CDDF}}$ differed from the HM12 model by a factor of ~ 5 within their simulations. Christiansen et al. (2020) recently revised this discrepancy downward by a factor of ~ 2 by invoking IGM heating associated with jet feedback in the SIMBA simulation. This revised estimate is in better agreement with the smaller factor of ~ 2 discrepancy noted

³ We choose to match the CDDF over a limited range in N_{HI} , rather than matching the mean or distribution of the Ly α forest transmission, as the CDDF is less susceptible to systematic uncertainties associated with signal-to-noise and the uncertain properties of high density gas in the CGM. Nevertheless, we note the mean transmission associated with the rescaled CDDF – given in Table 1 – is in excellent agreement with $\langle F \rangle = 0.983 \pm 0.009$ at $\langle z \rangle = 0.08$ from Kim et al. (2021) and the flux decrement $D_{\text{A}}(z) = 1 - \langle F \rangle = 0.014(1+z)^{2.2 \pm 0.2}$ from Shull et al. (2015).

by other independent studies (Wakker et al. 2015; Shull et al. 2015; Gaikwad et al. 2017a; Viel et al. 2017), although for different reasons, as these models did not include jet feedback. In this work we find a difference of at most a factor of ~ 1.7 compared to HM12 for our fiducial AGN feedback and no feedback models (H02), which is within the factor of ~ 2 uncertainty expected in UV background models (e.g. Khaire & Srianand 2015; Faucher-Giguère 2020). The additional hot gas in the StrongAGN model decreases the $\Gamma_{\text{HI}}^{\text{CDDF}}$ by a further factor of ~ 2 relative to our fiducial AGN and H02 simulations, which is also in good agreement with the relative change found by Christiansen et al. (2020) when comparing the SIMBA jet and no-jet feedback models.⁴ Sufficiently potent AGN feedback that heats the low density IGM can therefore relax the requirement on the number of ionising photons that was first pointed out by Kollmeier et al. (2014), although in contrast to Christiansen et al. (2020), we find this additional heating is not necessarily required. Blazar heating has a qualitatively similar effect on the required $\Gamma_{\text{HI}}^{\text{CDDF}}$ to strong AGN feedback, as was also noted by Kollmeier et al. (2014) (see their fig. 3).

Following the rescaling of the column densities, all four models in the left panel of Fig. 3 are in good agreement (i.e. within $\sim 1-1.5\sigma$) with the observed CDDF at $10^{13.3} \text{ cm}^{-2} \leq N_{\text{HI}} \leq 10^{14.5} \text{ cm}^{-2}$. Note again that at column densities $N_{\text{HI}} \lesssim 10^{13.3} \text{ cm}^{-2}$ the CDDF is incomplete and is dependent on the assumed signal-to-noise (see Appendix B). Comparing the H02 and StrongAGN models, we find that strong AGN feedback can alter the shape and amplitude of the CDDF. This is in agreement with earlier work by Gurvich et al. (2017), although differences between the models are within $\sim 1\sigma$ at the column densities, $N_{\text{HI}} \geq 10^{13.3} \text{ cm}^{-2}$, where the COS data are complete. With a higher precision measurement of the CDDF, it may therefore be possible to use the slope of the CDDF around $N_{\text{HI}} \sim 10^{14} \text{ cm}^{-2}$ to distinguish between different feedback models. We note, however, that the differences between H02 (no feedback) and our fiducial AGN model are very small at $N_{\text{HI}} \geq 10^{13.3} \text{ cm}^{-2}$, and are comparable to those found by Nasir et al. (2017) and Viel et al. (2017), reiterating their finding that AGN feedback plays a negligible role in changing the amplitude of the CDDF for our fiducial AGN feedback model. We therefore conclude that the extent to which AGN feedback and galaxy formation impact on the CDDF will depend on the specifics of the (uncertain) sub-grid modelling. In contrast our earlier work (Viel et al. 2017; Nasir et al. 2017), however, we find better agreement between the simulated and observed CDDF at $10^{14} \text{ cm}^{-2} < N_{\text{HI}} \leq 10^{14.5} \text{ cm}^{-2}$. The main reason for this improvement is that the simulations in this work have higher mass resolution and include a correction to the CDDF for both box size and mass resolution (see Appendix A).

Finally, in the right panel of Fig. 3 we show the Doppler parameter distribution. As has been noted previously, the simulated line widths are narrower than the observations (Gaikwad et al. 2017b; Nasir et al. 2017). The observed Doppler parameter distribution peaks in the bin at $b = 27.5 \pm 2.5 \text{ km s}^{-1}$ (see also Danforth et al. 2010, 2016), whereas the simulated distributions all peak at $b = 22.5 \pm 2.5 \text{ km s}^{-1}$, corresponding to thermally broadened lines with $T \simeq 10^{4.5} \text{ K}$. More quantitatively, the AGN (H02) simulations exceed the observed distribution by 4.6σ (5.8σ) at $b = 22.5 \pm 2.5 \text{ km s}^{-1}$. Interestingly, this

discrepancy also holds for the StrongAGN and Blazar heating models. The explanation for this was outlined in Viel et al. (2017); the additional hot gas in the WHIM does not produce Ly α absorption at the necessary column densities, since that gas is typically hot ($T \sim 10^6 \text{ K}$) and collisionally ionised. Hence, while strong AGN feedback that efficiently heats the low density IGM can alleviate differences between the observed and simulated CDDF and the mean transmission $\langle F \rangle$ (in agreement with Christiansen et al. 2020), unless this feedback is tuned to produce gas at just the right density and temperature, it will not reproduce the number of lines with $b \lesssim 30 \text{ km s}^{-1}$ in the Ly α forest at $z = 0.1$ (Viel et al. 2017). Lastly, the black dashed curve in Fig. 3 provides a crude estimate of the additional line broadening required for consistency with the COS data at $b \lesssim 30 \text{ km s}^{-1}$, where we show that a factor 1.24 increase to the H02 model line widths achieves much better agreement. A 1.5σ discrepancy at $b \sim 42.5 \pm 2.5 \text{ km s}^{-1}$ remains, possibly indicating there is also a lack of $T \sim 10^5 \text{ K}$ gas in the simulations. As we demonstrate later, however, this difference does not preclude a statistically acceptable fit to the data.

4 THERMAL AND TURBULENT LINE BROADENING

4.1 The thermal asymptote at $z \leq 0.5$

Since we argue that our AGN feedback models fail to explain the observed line widths in the Ly α forest at $z \simeq 0.1$, we now turn to consider alternatives. One possible explanation for the discrepancy between the simulated and observed Doppler parameter distribution is increased photoheating associated with a hardening of the UV background spectrum. The resulting enhancement to the IGM temperature produces additional thermal broadening in the Ly α forest. Indeed, additional photoheating is typically invoked to explain the IGM temperature boost inferred from the Ly α forest at $z \simeq 3$ (Schaye et al. 2000; Ricotti et al. 2000; Becker et al. 2011; Walther et al. 2019), when the rising contribution to the ionising emissivity from quasars is thought to harden the UV background spectrum and drive HeII reionisation (Theuns et al. 2002a; Bolton et al. 2009; Puchwein et al. 2015; Upton Sanderbeck et al. 2016). An interesting question is then: how hard would the UV background spectrum need to be to achieve consistency between the observed COS line widths and theoretical models? More importantly, is the required spectral hardening physically plausible?

In the canonical model, the IGM is expected to follow a power-law temperature-density relation following reionisation, $T = T_0 \Delta^\gamma$, with some additional scatter around this relation due to shock heating (Hui & Gnedin 1997; McQuinn & Upton Sanderbeck 2016). This arises due to photoheating and adiabatic cooling for densities $\Delta \lesssim 10$. At late times the slope of this relation approaches $T \propto \Delta^{1/1.72} \simeq \Delta^{0.58}$, where the exponent $\gamma - 1 = 0.58$ arises through the temperature dependence of the case-A recombination coefficient for hydrogen, $\alpha_A \propto T^{-0.72}$ (see e.g. Miralda-Escudé & Rees 1994; McQuinn & Upton Sanderbeck 2016). The temperature-density relation furthermore retains no memory of its earlier reionisation and heating history $\Delta z \sim 1-2$ after HI reionisation at $z \simeq 6$ or HeII reionisation at $z \simeq 3$. Once this ‘‘thermal asymptote’’ is reached and the IGM is in photoionisation equilibrium, the IGM temperature is set only by the spectral shape of the UV background (Hui & Haiman 2003), and is independent of the UV background intensity.

This is further illustrated in the Fig. 4, where we perform a non-equilibrium ionisation calculation to obtain the temperature of a hydrogen and helium gas parcel that is reionised by a time indepen-

⁴ Note the mass fraction in the diffuse IGM and WHIM for the StrongAGN (AGN) models are very similar to the Jet (No-Jet) models presented by Christiansen et al. (2020) which have 16.4 (38.8) per cent and 70.5 (28.7) per cent of the baryon mass in the diffuse IGM and WHIM, respectively (cf. Table 2 in this work).

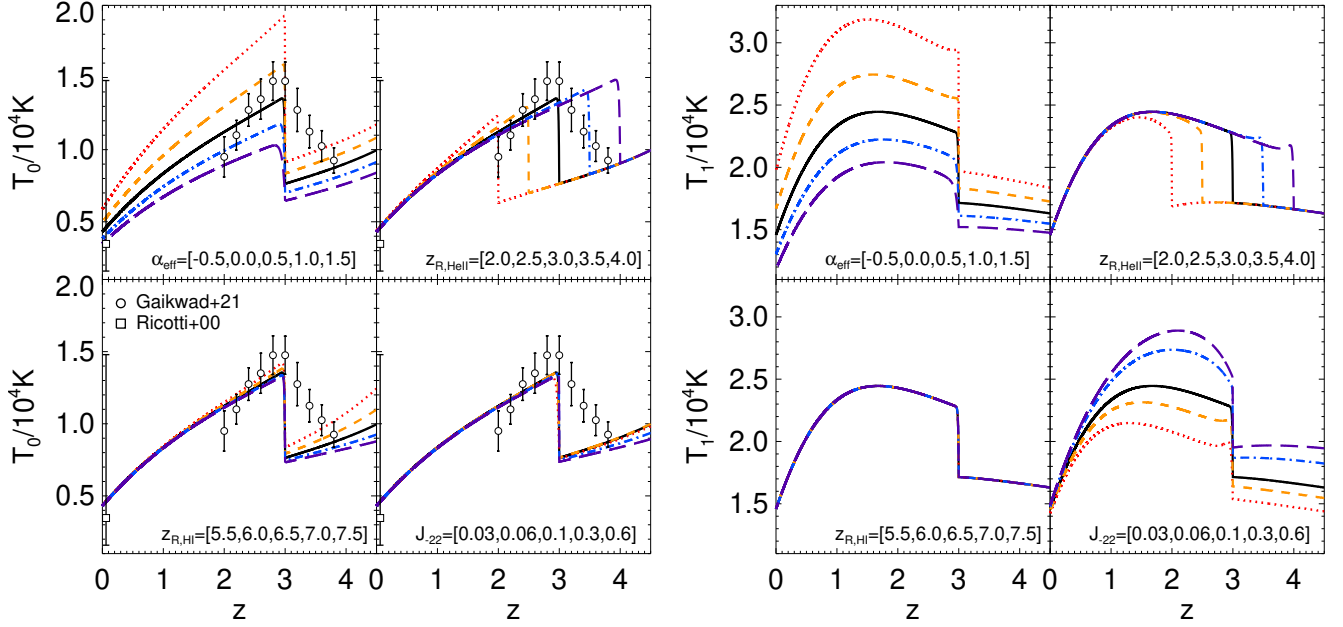


Figure 4. *Left:* Temperature evolution with redshift for a gas parcel at the mean density, $\Delta = 1$, that has been photoionised and heated by a power-law UV spectrum, $J_E \propto E^{-\alpha_{\text{eff}}}$. Individual panels show the effect of varying different parameters on T_0 . Clockwise from the top left, these are: the effective power-law spectral index, α_{eff} , the redshift of HeII reionisation, $z_{\text{R,HeII}}$, the specific intensity at the Lyman limit, $J_{-22} = J_{13.6\text{eV}}/10^{-22} \text{ erg s}^{-1} \text{ cm}^{-2} \text{ sr}^{-1} \text{ Hz}^{-1}$, and the redshift of HI reionisation, $z_{\text{R,HI}}$. The central parameter values, corresponding to the black curves in each sub-panel, are $\alpha_{\text{eff}} = 0.5$, $z_{\text{R,HI}} = 6.5$, $z_{\text{R,HeII}} = 3.0$ and $J_{-22} = 0.1$. Note that the temperature at $z \leq 0.5$ depends only on the spectral index. For comparison, temperature measurements from the Ly α forest at $2 \leq z \leq 3.8$ are shown as open circles (Gaikwad et al. 2021), and at $z = 0.06$ by an open square (Ricotti et al. 2000). *Right:* As for the left panel, but now for a gas parcel with $\Delta = 10$, similar to the densities typically probed by the $z = 0.1$ Ly α forest. Note the different scale on the vertical axis compared to the left panel.

dent UV background. The results are displayed at two gas densities, $\Delta = 1$ (left panels) and $\Delta = 10$ (right panels), i.e. at the mean density and the density where most of the Ly α forest absorption at $z = 0.1$ occurs for $10^{13.3} \text{ cm}^{-2} \leq N_{\text{HI}} \leq 10^{14.5} \text{ cm}^{-2}$. We include the effect of photoionisation and photoheating, collisional ionisation, radiative cooling, adiabatic cooling and secondary ionisations by fast electrons, following the equations given in appendix B of Šoltinsky et al. (2021). The spectrum of the ionising radiation is treated as a single power-law, $J_E \propto E^{-\alpha_{\text{eff}}}$, with effective⁵ spectral index α_{eff} . For the photons with energies $13.6\text{eV} \leq E < 54.4\text{eV}$ that are capable of HI and HeI ionisation, we assume a specific intensity

$$J_E = \begin{cases} J_{13.6\text{eV}} \left(\frac{E}{13.6\text{eV}}\right)^{-\alpha_{\text{eff}}} & \text{for } z < z_{\text{R,HI}}, \\ 0 & \text{for } z \geq z_{\text{R,HI}}, \end{cases} \quad (1)$$

where $z_{\text{R,HI}}$ is the redshift of (instantaneous) HI and HeI reionisation. For the higher energy photons, $E \geq 54.4\text{eV}$, responsible for HeII reionisation, we instead assume

$$J_E = \begin{cases} J_{13.6\text{eV}} 4^{-\alpha_{\text{eff}}} \left(\frac{E}{54.4\text{eV}}\right)^{-\alpha_{\text{eff}}} & \text{for } z < z_{\text{R,HeII}}, \\ 0 & \text{for } z \geq z_{\text{R,HeII}}, \end{cases} \quad (2)$$

where $z_{\text{R,HeII}}$ is the redshift of (instantaneous) HeII reionisation.

Clockwise from the top left in each sub-panel of Fig. 4, we vary the spectral index α_{eff} , the redshift of HeII reionisation

$z_{\text{R,HeII}}$, the intensity of the UV background at the HI Lyman limit, $J_{-22} = J_{13.6\text{eV}}/10^{-22} \text{ erg s}^{-1} \text{ cm}^{-2} \text{ Hz}^{-1} \text{ sr}^{-1}$, and the redshift of HI reionisation, $z_{\text{R,HI}}$. We adopt ranges for each parameter that bracket the plausible values: the bulk of HI and HeII reionisation should be complete by $z \simeq 6$ (Yang et al. 2020) and $z \simeq 3$ (Worseck et al. 2019), respectively, while typical values in UV background models at $z = 0.1$ are $\alpha_{\text{eff}} \simeq 1.0\text{--}1.4$ (see Fig. 5) and $J_{-22} \simeq 0.2$ (Puchwein et al. 2019; Khaire & Srianand 2019; Faucher-Giguère 2020).

The results for $\Delta = 1$ in Fig. 4 (left panel) encompass the recent IGM temperature measurements at the mean density, T_0 , from Gaikwad et al. (2021), who use a variety of different statistical measures of the Ly α forest transmitted flux to obtain joint constraints on T_0 and γ at $2 \leq z \leq 3.8$. The models are also consistent with the only IGM temperature measurement to date from the Ly α forest at $z \simeq 0$ (Ricotti et al. 2000), although the error bars on this measurement are large (see their fig. 12). Note, however, our aim is not to match these data points; a single zone reionisation model will in any case not correctly capture the volume averaged gas temperature during inhomogeneous HeII reionisation at $z \simeq 3$ (see e.g. Upton Sanderbeck et al. 2016; Upton Sanderbeck & Bird 2020). The important point, as we now discuss below, is that this approach captures the *late time behaviour* of the IGM temperature when it tracks the thermal asymptote (cf. Hui & Haiman 2003).

First, note that Fig. 4 shows the gas temperatures in the low density IGM at $z < 0.5$ follow a single thermal asymptote, as expected. This implies a temperature sensitive statistic, such as the Doppler parameter distribution, should provide an excellent constraint on the spectral shape of the UV background at $z \simeq 0$ if the low column density Ly α forest is primarily thermally broadened by photo-

⁵ We refer to this as an effective spectral index, as in reality the spectral shape of the UV background will be modified by intervening absorption and recombination emission from the IGM, even if the intrinsic spectrum emitted by the ionising source population is a pure power-law. See e.g. the right panel of Fig. 7, which we discuss later.

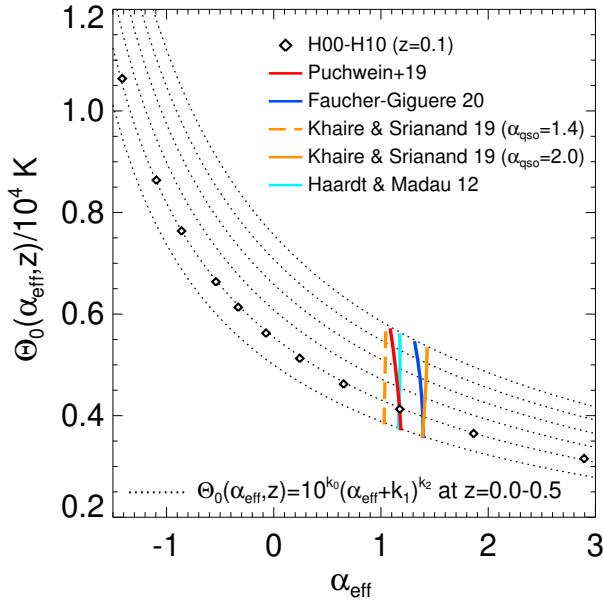


Figure 5. The temperature at the mean density along the thermal asymptote, Θ_0 , as a function of the effective power-law spectral index, α_{eff} , for a hydrogen and helium gas parcel heated by a power-law ionising spectrum with specific intensity $J_E \propto E^{-\alpha_{\text{eff}}}$. The dotted curves are obtained at intervals of $\Delta z = 0.1$ from $z = 0.0$ (lower curve) to $z = 0.5$ (upper curve) using Eq. (3). The black diamonds assume $\Theta_0 = T_0$ at $z = 0.1$ for the hydrodynamical simulations H00–H10 listed in Table 1. The solid and dashed curves show the thermal asymptote predicted by various UV background models: Puchwein et al. (2019) (solid red curve), Faucher-Giguère (2020) (solid blue curve), Khaire & Srianand (2019) for a quasar contribution with spectral index $\alpha_{\text{qso}} = 1.4$ (dashed orange curve) or $\alpha_{\text{qso}} = 2.0$ (solid orange curve), and Haardt & Madau (2012) (solid cyan curve). The empirically calibrated UV background models all predict thermal asymptotes in a narrow range, consistent with $\alpha_{\text{eff}} = 1.0$ – 1.4 .

heating.⁶ It is convenient to provide a fit to the temperature at the thermal asymptote at the mean density, Θ_0 , as a function of α_{eff} at $0 \leq z \leq 0.5$. Our numerical results from the non-equilibrium ionisation calculations are well approximated by

$$\Theta_0(\alpha_{\text{eff}}, z) = 10^{k_0(z)} \text{K} [\alpha_{\text{eff}} + k_1(z)]^{k_2(z)}, \quad (3)$$

where the redshift dependent coefficients k_0 , k_1 and k_2 are listed in Table 3. Eq. (3) reproduces our numerical calculation to within 1 per cent for $-1.5 \leq \alpha_{\text{eff}} \leq 3.0$. The thermal asymptote at $\Delta = 10$ is furthermore similarly well approximated by $\Theta_1(\alpha_{\text{eff}}) = 3.27\Theta_0(\alpha_{\text{eff}})$ at $z = 0.1$.

We can therefore use Eq. (3) to estimate the effective power-law spectra indices, α_{eff} , that are *equivalent* to the spectral shape assumed in different synthesis models for the metagalactic UV background (Haardt & Madau 2012; Khaire & Srianand 2019; Puchwein

⁶ Note, however, that in photoionisation equilibrium the gas temperature at densities $\Delta \gtrsim 10$ will become increasingly sensitive to the spectral shape and specific intensity of the UV background, as the dominant gas cooling mechanism transitions from adiabatic to radiative cooling. In this regime, lowering J_{-22} produces colder gas temperatures, since the H I collisional excitation cooling rate scales as $\sim n_{\text{HI}}$. For gas with $\Delta = 100$ at $z \sim 0.1$ ($N_{\text{HI}} \sim 10^{15} \text{ cm}^{-2}$) the range of temperatures that result from $J_{-22} = 0.03$ – 0.6 in our single zone model becomes comparable to the range of temperatures for $\alpha_{\text{eff}} = -0.5$ – 1.5 .

Table 3. Coefficients for the best fit to the thermal asymptote, Θ_0 , obtained using Eq. (3) at redshifts $0.0 \leq z \leq 0.5$ for a power-law UV background spectrum with $J_E \propto E^{-\alpha_{\text{eff}}}$. The fits reproduce the numerical calculation to within 1 per cent for $-1.5 \leq \alpha_{\text{eff}} \leq 3.0$.

Redshift, z	k_0	k_1	k_2
0.0	3.976	2.412	−0.725
0.1	4.022	2.413	−0.727
0.2	4.063	2.414	−0.729
0.3	4.099	2.415	−0.732
0.4	4.131	2.416	−0.734
0.5	4.161	2.417	−0.737

et al. 2019; Faucher-Giguère 2020). In Fig. 5, the black dotted curves show Eq. (3) at $z = 0$ – 0.5 . The Θ_0 values predicted at $z = 0.0$ – 0.5 by the UV background synthesis models are shown by the (roughly vertical) solid and dashed curves in Fig. 5, where we have again calculated the temperatures using our non-equilibrium ionisation code. For comparison, the black diamonds show $\Theta_0 \simeq T_0$ at $z = 0.1$ for the hydrodynamical simulations H00–H10 listed in Table 1.

Note that the gas temperatures at $\Delta = 1$ predicted by the UV background models are all within a very narrow temperature range, $\Theta_0 \simeq 3950 \text{ K}$ – 4250 K ($\Theta_1 \simeq 12920 \text{ K}$ – 13900 K) at $z = 0.1$, which from Eq. (3) is equivalent to a spectrum with an effective power-law slope of $\alpha_{\text{eff}} = 1.0$ – 1.4 . This is expected, as at least half (and possibly all, depending on the assumed spectral shape) of the contribution to the UV background at $z \simeq 0$ is thought to be from quasars and active galactic nuclei (e.g., Kulkarni et al. 2019; Shen et al. 2020). The UV background models from Khaire & Srianand (2019) adopt the hardest (softest) *intrinsic* quasar spectrum of $\alpha_{\text{qso}} = 1.4$ ($\alpha_{\text{qso}} = 2.0$), shown by the dashed (solid) orange curves in Fig. 5. We find the gas temperatures predicted by these models correspond to hardened⁷ effective spectral indices of $\alpha_{\text{eff}} = 1.03$ and $\alpha_{\text{eff}} = 1.40$, respectively. For comparison, the Puchwein et al. (2019) and Faucher-Giguère (2020) models both assume $\alpha_{\text{qso}} = 1.7$, but predict temperatures consistent with $\alpha_{\text{eff}} = 1.17$ and $\alpha_{\text{eff}} = 1.40$, respectively; the precise amount of hardening is dependent on the different IGM opacity models used in these synthesis UV background models. Finally, Haardt & Madau (2012) assume $\alpha_{\text{qso}} = 1.57$, but their UVB model predicts temperatures consistent with $\alpha_{\text{eff}} = 1.17$. Overall, this implies a modest spectral hardening of $\alpha_{\text{eff}} - \alpha_{\text{qso}} \simeq -0.5$ associated with the propagation of the ionising photons through the IGM.

For comparison, Lusso et al. (2015) measure an extreme-UV spectral index of $\alpha_{\text{qso}} = 1.70 \pm 0.61$ at $600 \text{ \AA} \leq \lambda \leq 912 \text{ \AA}$ from a stacked spectrum of 53 luminous quasars at $z = 2.4$, while Stevans et al. (2014) obtain $\alpha_{\text{qso}} = 1.41 \pm 0.15$ at $500 \text{ \AA} \leq \lambda \leq 1000 \text{ \AA}$, from 159 AGN with $\langle z \rangle = 0.37$. However, in an analysis of 11 AGN at $1.45 \leq z \leq 2.14$, Tilton et al. (2016) find a harder spectral index $\alpha_{\text{qso}} = 0.72 \pm 0.26$ at $450 \text{ \AA} \leq \lambda \leq 770 \text{ \AA}$ (see also Scott et al. 2004). Hence, if taking the intrinsic quasar spectral index from Stevans

⁷ This hardening is due to the combined effect of the He II opacity of the IGM and the rapidly declining UVB emissivity at $z < 1$. The mean free path at the He II ionisation edge ($E = 54.4 \text{ eV}$) is $\sim 500 \text{ pMpc}$ by $z \sim 1$ (see fig. 1 in Puchwein et al. 2019), so a non-negligible fraction of the $z \sim 0$ UVB at $E \sim 54.4 \text{ eV}$ is produced by redshifted photons emitted at higher energies. The average excess energy per He II photoionisation is therefore significantly increased above that expected for an optically thin IGM at $z \sim 0$ (see fig. 3 in Puchwein et al. 2019). By contrast, the UVB spectrum between $13.6 \text{ eV} < E < 54.4 \text{ eV}$ can instead slightly soften as a result of IGM processing (Shull & Danforth 2020).

et al. (2014) (consistent with the $\alpha_{\text{qso}} = 1.4$ model from Khaire & Srianand (2019), a plausible hardness limit for quasar dominated UV background models is approximately $\alpha_{\text{eff}} \simeq 1$, yielding $\Theta_0 \simeq 4300$ K ($\Theta_1 \simeq 14050$ K) for the thermal asymptote at $z = 0.1$. A more extreme case is possible if instead adopting the harder Tilton et al. (2016) composite spectrum and once again assuming some spectral hardening at the He II edge, such that $\alpha_{\text{eff}} - \alpha_{\text{qso}} \simeq -0.5$. If taking the lower bound of the Tilton et al. (2016) 1σ measurement, we obtain $\alpha_{\text{eff}} \simeq 0$, yielding $\Theta_0 \simeq 5550$ K ($\Theta_1 \simeq 18150$ K). We caution, however, the Tilton et al. (2016) composite spectrum may be less reliable than Stevans et al. (2014) due their use of low resolution COS/G140L spectra and their small sample size. In either case, as we will demonstrate in Section 5, an IGM heated by a UV background spectrum with $0 < \alpha_{\text{eff}} < 1$ would still be too cold to reproduce the COS Ly α line width distribution in our simulations in the absence of any additional non-thermal broadening.

4.2 Unresolved non-thermal broadening

An alternative to increasing the thermal widths of the Ly α absorbers is the introduction of (unresolved) non-thermal broadening in hydrodynamical simulations of the IGM (e.g. Oppenheimer & Davé 2009; Gaikwad et al. 2017b). We can make a crude estimate of the turbulent contribution needed to reproduce the COS Doppler parameter distribution using the approach introduced by Oppenheimer & Davé (2009). Let there be an unresolved (i.e. sub-grid) turbulent component in the simulated Ly α absorbers, where

$$b_{\text{turb}}^2 = b_{\text{obs}}^2 - b_{\text{noturb}}^2. \quad (4)$$

Here b_{turb} is the turbulent contribution to the Doppler parameters, b_{obs} are the observed Doppler parameters in the COS data, and b_{noturb} are the Doppler parameters obtained from our simulated spectra. Defining $\xi = b_{\text{obs}}/b_{\text{noturb}}$, Eq. (4) then becomes

$$b_{\text{turb}} = (\xi^2 - 1)^{1/2} b_{\text{noturb}}. \quad (5)$$

We may now estimate the b_{turb} required to match the COS line widths by taking the photoheating in our fiducial UVB model ($\alpha_{\text{eff}} = 1.17$) as an effective prior on the gas temperature. From the black dashed curve in the right panel of Fig. 3, we will assume a boost to the line widths of $\xi = b_{\text{obs}}/b_{\text{noturb}} \simeq 1.24$ will allow the AGN and H02 simulations to approximately match the COS data. From Eq. (5), this corresponds to a turbulent Doppler parameter contribution of $b_{\text{turb}} \simeq 0.73 b_{\text{noturb}}$.

It is also instructive to have an estimate for b_{turb} as a function of column density, N_{HI} . Here we make use of the fact that the narrowest Ly α line widths associated with gas on the temperature-density relation in the diffuse IGM at $z \simeq 0.1$ are thermally broadened (see Fig. 2 and associated discussion). Assuming $b_{\text{noturb}} \simeq b_{\text{therm}}$ for these absorbers, Eq. (4) then becomes

$$b_{\text{turb}} = (\xi^2 - 1)^{1/2} \left(\frac{2k_{\text{B}}T}{m_{\text{H}}} \right)^{1/2}. \quad (6)$$

Next, assuming the size of Ly α forest absorbers is set by the local Jeans scale in the IGM (Schaye 2001; Garzilli et al. 2015), a power law relationship between N_{HI} and density will hold,

$$N_{\text{HI}} = N_{\text{HI},0} \Delta^\beta, \quad (7)$$

where $\beta = 1.72 - 0.22\gamma$ for $T = T_0 \Delta^{\gamma-1}$ and a case-A recombination coefficient⁸ $\alpha_{\text{A}} \simeq 4.06 \times 10^{-13} \text{ cm}^3 \text{ s}^{-1} (T/10^4 \text{ K})^{-0.72}$. For our

⁸ The power-law approximation for α_{A} given here reproduces the more ac-

AGN simulation, we find a best fit value of $N_{\text{HI},0} = 10^{12.12} \text{ cm}^{-2}$, assuming $\beta = 1.37$ for $\gamma = 1.58$. Combining Eq. (7) and Eq. (6), and once again assuming a power-law temperature density relation, we obtain

$$b_{\text{turb}} = (\xi^2 - 1)^{1/2} \left(\frac{2k_{\text{B}}T_0}{m_{\text{H}}} \right)^{1/2} \left(\frac{N_{\text{HI}}}{N_{\text{HI},0}} \right)^{(\gamma-1)/2\beta}, \quad (8)$$

Evaluating Eq. (8) for the AGN model at $N_{\text{HI}} = 10^{13.5} \text{ cm}^{-2}$ assuming $\xi = 1.24$ then gives a density dependent turbulent contribution of

$$b_{\text{turb}} \simeq 12.1 \text{ km s}^{-1} \left(\frac{N_{\text{HI}}}{10^{13.5} \text{ cm}^{-2}} \right)^{0.21}, \quad (9)$$

for the Ly α absorbers with $10^{13.3} \text{ cm}^{-2} \leq N_{\text{HI}} \leq 10^{14.5} \text{ cm}^{-2}$ associated with gas on the power-law temperature-density relation. The required turbulent velocity component along the line of sight is then $v_{\text{turb}} = b_{\text{turb}}/\sqrt{2} \simeq 8.5 \text{ km s}^{-1} (N_{\text{HI}}/10^{13.5} \text{ cm}^{-2})^{0.21}$. This gives an approximate upper limit on the turbulent contribution to the narrowest, thermally broadened Ly α lines arising from the coldest gas in the diffuse IGM at $z \sim 0.1$.

5 RESULTS

5.1 Best fit Γ_{HI} and α_{eff} for the UV background at $z = 0.1$

We now proceed to perform a joint fit of our simulated spectra to the COS measurements of the CDDF and Doppler parameter distribution. We vary two model parameters in our analysis: the meta-galactic H I photoionisation rate, Γ_{HI} , and the effective power-law spectral index of the UV background, α_{eff} . As discussed earlier, α_{eff} is directly related to the thermal asymptote at $z < 0.5$.

A grid of models is used for this fitting procedure. The line fits are obtained by performing a Voigt profile analysis on hydrodynamical simulations with 11 different α_{eff} values (H00-H10 in Table 1). For each of these simulations we also assume 7 different photoionisation rates ($0.4 - 1.0 \Gamma_{\text{HI},\text{P19}}$ in steps of 0.1). This gives a total of 77 separate sets of mock Ly α forest spectra for Voigt profile fitting. The redshift path length of each set is $\Delta z = 210.1$.

We furthermore consider two different cases in our analysis (i.e. we actually fit 2×77 sets of mocks). These two cases assume $b_{\text{turb}} = 0$ (i.e no additional turbulent broadening, $\xi = 1$) and $b_{\text{turb}} = 0.73 b_{\text{noturb}}$ (i.e. $\xi = 1.24$), where for the latter we have followed the argument in Section 4.2 and assumed a prior limit on the thermal broadening of the Ly α absorbers.⁹

A χ^2 minimisation is then performed on the COS data, such that

$$\chi^2 = \sum_i \sum_j [x_i(\Gamma_{\text{HI}}, \alpha_{\text{eff}}) - \mu_i] C_{ij}^{-1} [x_j(\Gamma_{\text{HI}}, \alpha_{\text{eff}}) - \mu_j], \quad (10)$$

where the vector \vec{x} is the Doppler parameter distribution and CDDF from the simulations, the vector $\vec{\mu}$ is the COS data, and C_{ij} is the COS data covariance matrix. However, the off-diagonal terms in the covariance matrix for the COS data are noisy, making the inversion of the covariance matrix difficult. We therefore assume the

curate fit from Verner & Ferland (1996) to within 10 per cent at $10^3 \text{ K} \leq T \leq 10^5 \text{ K}$.

⁹ In principle, we could also find a best fit sub-grid turbulent contribution to the line broadening by treating ξ as a free parameter. However, this would require fitting an additional grid of models in ξ for each of the 77 ($\alpha_{\text{eff}}, \Gamma_{\text{HI}}$) pairs, which would greatly increase the cost of the already time consuming Voigt profile fitting process. We leave this to future work.

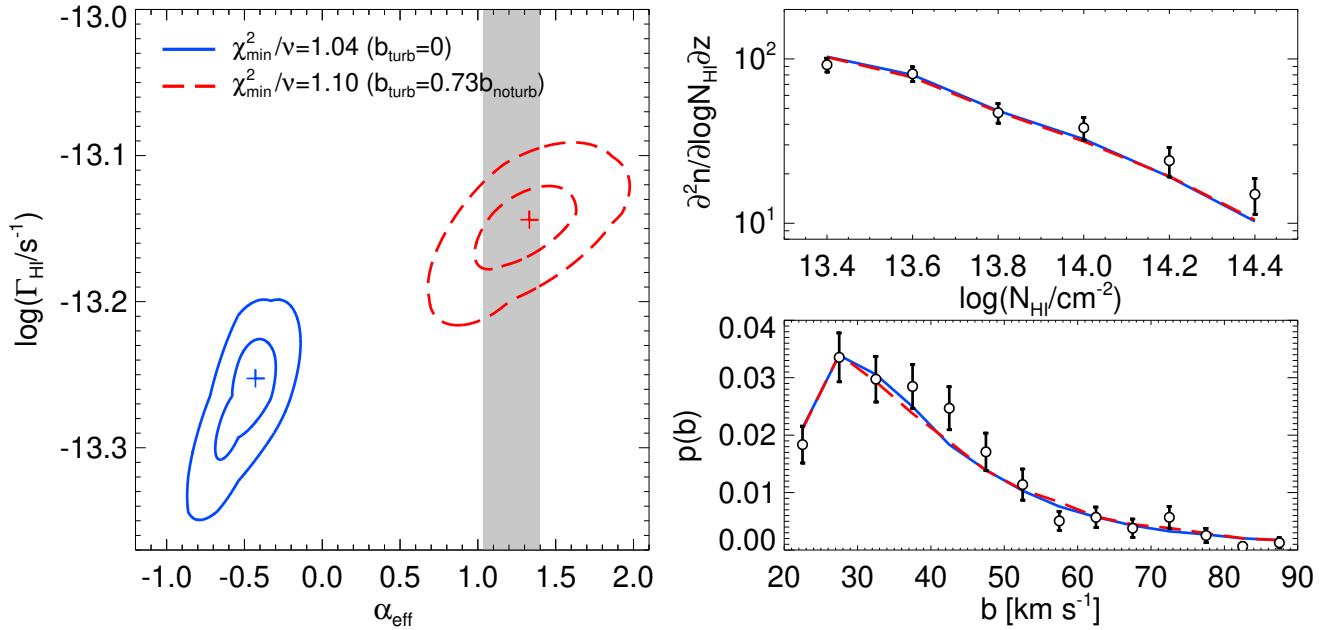


Figure 6. *Left:* The projection of χ^2 for the joint fit to the CDDF and Doppler parameter distribution including (red dashed curves) and excluding (blue solid curves) an additional turbulent contribution to the line widths (see Section 4.2 for details). The contours show $\Delta\chi^2 = \chi^2 - \chi^2_{\min} = 1$ and 4, corresponding to the 1σ and 2σ confidence intervals for the individual parameters Γ_{HI} and α_{eff} . The best fit model parameters (shown by the crosses) and 1σ uncertainties are $\log(\Gamma_{\text{HI}}/\text{s}^{-1}) = -13.25^{+0.03}_{-0.06}$ ($\log(\Gamma_{\text{HI}}/\text{s}^{-1}) = -13.14^{+0.02}_{-0.03}$) and $\alpha_{\text{eff}} = -0.43^{+0.13}_{-0.26}$ ($\alpha_{\text{eff}} = 1.33^{+0.30}_{-0.35}$) when excluding (including) the turbulent contribution to the line widths. For comparison, the grey shaded region shows the α_{eff} range consistent with the selection of UV background models shown in Fig. 5, $\alpha_{\text{eff}} \simeq 1.0\text{--}1.4$. Note that *the turbulent contribution has been deliberately calibrated for consistency with the grey band*. *Right:* The best fitting models to the CDDF and Doppler width distribution, compared to the COS data. The best fits have $\chi^2/\nu = 1.04$ (1.10) for $\nu = 18$ degrees of freedom excluding (including) the turbulent contribution, with a probability that the χ^2 may be exceeded randomly of $p = 0.41$ ($p = 0.35$).

COS data and the AGN model have similar covariance properties. If the simulated covariance matrix is C_{ij}^s , the correlation coefficients are $r_{ij}^s = C_{ij}^s/[C_{ii}^s C_{jj}^s]^{1/2}$. The off-diagonal terms in the covariance matrix for the COS data can then be estimated from the observed diagonal elements and the simulated correlation coefficients, such that $C_{ij} = r_{ij}^s [C_{ii} C_{jj}]^{1/2}$ (Lidz et al. 2006).

The resulting best fit parameters are displayed in the left panel of Fig. 6, where the $\Delta\chi^2$ contours are shown for no additional turbulent contribution to the Ly α forest (blue solid curves) and including our simple estimate for an additional, unresolved turbulent velocity (red dashed curves). For comparison, the grey shaded region show the effective spectral index, α_{eff} , predicted by various UV background models (Haardt & Madau 2012; Khaire & Srianand 2019; Puchwein et al. 2019; Faucher-Giguère 2020). Note again *the turbulent contribution has been chosen by hand* so that the grey region and red contours in Fig. 6 intersect.

There is a degeneracy line between Γ_{HI} and α_{eff} in Fig. 6, where a softer spectrum leads to larger Γ_{HI} , and vice versa. This is because, in photoionisation equilibrium, the HI column density scales as $N_{\text{HI}} \propto T_0^{-0.22}/\Gamma_{\text{HI}}$ (Schaye 2001) and, from Eq. (3), the IGM temperature decreases for a softer ionising spectrum (this is also exemplified by the behaviour of $\Gamma_{\text{HI}}^{\text{CDDF}}$ in Table 1). The best fit models excluding (including) a turbulent contribution are shown in the right panel of Fig. 6, and have $\chi^2/\nu = 1.04$ ($\chi^2/\nu = 1.10$) for $\nu = 18$ degrees of freedom, with a probability that the χ^2 may be exceeded randomly of $p = 0.41$ ($p = 0.35$). The corresponding best fit parameters and 1σ (statistical) uncertainties are $\log(\Gamma_{\text{HI}}/\text{s}^{-1}) = -13.25^{+0.03}_{-0.06}$ ($\log(\Gamma_{\text{HI}}/\text{s}^{-1}) = -13.14^{+0.02}_{-0.03}$) and $\alpha_{\text{eff}} = -0.43^{+0.13}_{-0.26}$ ($\alpha_{\text{eff}} = 1.33^{+0.30}_{-0.35}$). From Eq. (3), this is equivalent to a thermal

asymptote with $\Theta_0 = 6390^{+680}_{-290}$ K ($\Theta_0 = 4030^{+300}_{-220}$ K), or for gas at $\Delta = 10$, $\Theta_1 = 20900^{+2220}_{-950}$ K ($\Theta_1 = 13180^{+980}_{-720}$ K).

In Fig. 7, these results are compared to the predictions from UV background models and independent observational constraints on the metagalactic photoionisation rate, Γ_{HI} . Our constraints on Γ_{HI} in the left panel of Fig. 7 are consistent with the measurements from Gaikwad et al. (2017a) and Khaire et al. (2019) at $z = 0.1$ from the probability distribution function (PDF) and/or power spectrum of the Ly α forest transmission. Our best fit values are a factor of 0.6–0.8 times the Puchwein et al. (2019) model and a factor of 1.6–2.0 times larger than Haardt & Madau (2012) (see also the discussion of $\Gamma_{\text{HI}}^{\text{CDDF}}$ in Section 3.2). However, the 1σ uncertainties in this work are a factor of $\sim 3\text{--}4$ smaller than the earlier studies. This is partly because we have not included systematic uncertainties from continuum fitting and the assumed cosmology, that may (conservatively) double the size of the error bar on Γ_{HI} (see e.g. table 8 in Gaikwad et al. 2017a). However, another reason is that the joint analysis of the CDDF and Doppler parameter distribution is effective at breaking the degeneracy between Γ_{HI} and the thermal state of the IGM.

Our constraints on α_{eff} are shown in the right hand panel of Fig. 7, and are compared to various UV background models. By design, the model with turbulent broadening, $b_{\text{turb}} = 0.73 b_{\text{noturb}}$, is in very good agreement with the spectral shape of UV background models close to the Lyman limit. However, the constraint on α_{eff} for $b_{\text{turb}} = 0$ yields an unphysically hard spectral shape for the UV background and differs from our fiducial $\alpha_{\text{eff}} = 1.17$ model (Puchwein et al. 2019) by $\sim 6\text{--}7\sigma$. It is possible that existing UV background models have spectral shapes that are still slightly too soft, although given the wide range of observables at different redshifts these models cali-

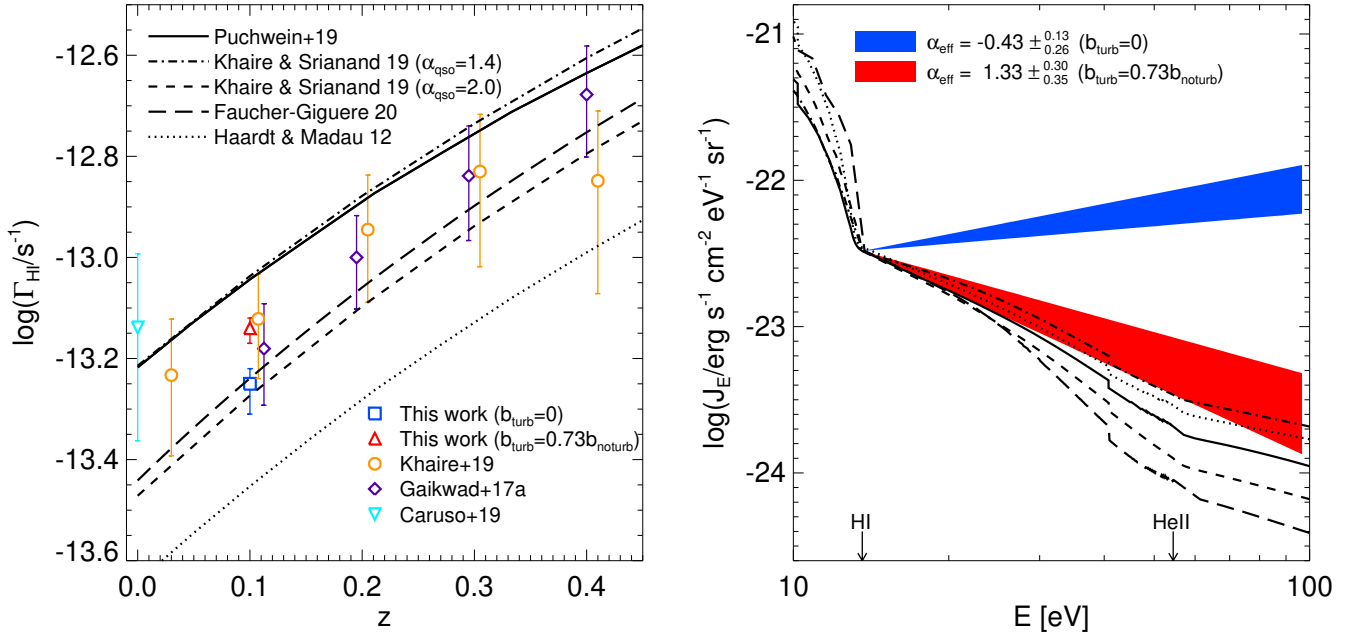


Figure 7. *Left:* The metagalactic H I photoionisation rate, Γ_{HI} , at $z < 0.5$. The results of this work are shown by the blue square (red triangle) excluding (including) an additional unresolved turbulent contribution to the Ly α line widths, $b_{\text{turb}} = 0.73b_{\text{noturb}}$. The curves show predictions for Γ_{HI} from the UV background synthesis models of Puchwein et al. (2019) (solid curve), Khaire & Srianand (2019) for $\alpha_{\text{qso}} = 1.4$ (dot-dashed curve) and $\alpha_{\text{qso}} = 2.0$ (short dashed curve), Faucher-Giguère (2020) (long dashed curve) and Haardt & Madau (2012) (dotted curve). Independent Γ_{HI} measurements are shown from a joint analysis of the power spectrum and PDF of the Ly α forest transmitted flux (Gaikwad et al. 2017a, purple diamonds), the power spectrum only (Khaire et al. 2019, orange circles), and from H α fluorescence in a galactic disc (Caruso et al. 2019, cyan inverted triangle). *Right:* The specific intensity, J_E , of the metagalactic UV background. The black curves show the UV background models displayed in the left panel, while the shaded blue (red) regions show our constraint on α_{eff} excluding (including) turbulent broadening. Note that the model with the turbulent contribution (red shading) has been deliberately calibrated for consistency with the spectral shape of the UV background models at the Lyman limit. To facilitate the comparison, all models have been normalised to match the amplitude of the Puchwein et al. (2019) spectrum at $E = 13.6$ eV. Vertical arrows show the location of the H I and He II ionisation edges at 13.6 eV and 54.4 eV.

brate to, as well as the good agreement between independent groups, we regard this as unlikely. Our statistical error bars may also underestimate the true uncertainty on α_{eff} . If, as previously discussed, we instead take $\alpha_{\text{eff}} = 0$ as a conservative limit on the hardness of the UV background spectrum at $z = 0.1$ (i.e. assuming it is dominated by emission from quasars with extreme UV spectral indices of $\alpha_{\text{qso}} \simeq 0.5$ (Scott et al. 2004; Tilton et al. 2016)), this differs by $\sim 2\sigma$ from our constraint of $\alpha_{\text{eff}} = -0.43^{+0.13}_{-0.26}$. This still suggests that photoheating by a hard UV background is disfavoured as the sole explanation for the observed line widths in the Ly α forest at $z = 0.1$.

5.2 Discussion

We now discuss the implications of our results. First, if – as we have argued – matching the COS line widths in the Ly α forest through photoheating by a hard UV background is unlikely, then if assuming a negligible turbulent component, what other (if any) heating processes might provide the requisite injection of energy? Upton Sanderbeck et al. (2016) demonstrated that the IGM thermal history is already well described by the photoheating expected from H I and He II reionisation at $z \geq 2.5$. Interestingly, however, they noted there may be room for an additional ~ 1 eV per proton at $\Delta \simeq 5$ by $z = 2$ (see their fig. 8), based on the IGM temperature measurements at $1.5 \leq z \leq 2.5$ from Boera et al. (2014). This suggests that any *additional* IGM heating process must be sub-dominant to the H I and He II photoheating before $z \simeq 2.5$.

We therefore take a similar approach to Upton Sanderbeck et al. (2016), where – based on the observed COS line widths – we estimate an upper limit for the additional energy injection into the IGM required at $z \leq 2.5$. The specific energy deposited into the IGM at $z_0 \leq z \leq z_{\text{R,H I}}$ from photoheating at overdensity $\Delta = \rho/\langle\rho\rangle$ is

$$u = \int_{z_0}^{z_{\text{R,H I}}} \frac{\mathcal{H}}{\rho} \frac{dz'}{H(z')(1+z')}, \quad (11)$$

where $\rho = \rho_{\text{crit}}\Omega_b\Delta(1+z)^3$, and for photoheating $\mathcal{H} = \sum_i n_i \varepsilon_i$, where n_i and ε_i are respectively the proper number density and photoheating rate for $i = [\text{H I}, \text{He I}, \text{He II}]$ (e.g. Nasir et al. 2016). Taking the Puchwein et al. (2019) UV background model (which is already calibrated to match existing IGM temperature measurements at $z > 2$ and has $\alpha_{\text{eff}} = 1.17$ at $z = 0.1$), we find boosting these model photoheating rates by a factor of 2 at $z \leq 2.5$ gives good agreement with the $\alpha_{\text{eff}} = -0.43^{+0.13}_{-0.26}$ (or equivalently the thermal asymptote temperature $\Theta_1 = 20900^{+2220}_{-950}$ K) we infer for $b_{\text{turb}} = 0$ in Section 5.1. From Eq. (11), this boost corresponds to an additional $u \simeq 6.9 \text{ eV m}_p^{-1}$ ($u \simeq 1.6 \text{ eV m}_p^{-1}$) injected into the IGM¹⁰ at $\Delta = 10$ ($\Delta = 1$) by $z_0 = 0.1$, *in excess* of that already provided by photoheating in the Puchwein et al. (2019) model. Note again, however, that

¹⁰ Note this is consistent with a density scaling of $u \propto \Delta^{1-0.72(\gamma-1)} \sim \Delta^{0.58}$ for $\gamma = 1.58$, which is the expectation for photoheating assuming the IGM is in photoionisation equilibrium.

this level of enhanced photoheating would require an unphysically hard UV background.

Any non-canonical heating process would therefore need to inject $\lesssim 6.9\text{eV m}_p^{-1}$ into $N_{\text{HI}} \simeq 10^{13.5}\text{cm}^{-2}$ absorbers by $z = 0.1$, while also having a negligible effect on the IGM temperature at $z > 2.5$. We now speculate on which processes are plausible. As already discussed, we find a volumetric heating process like blazar heating (Puchwein et al. 2012) with $u \propto \Delta^{-1}$ will not heat the IGM sufficiently at $\Delta \gtrsim 10$. A similar situation likely holds for Compton heating of the IGM by X-rays (Madau & Efstathiou 1999), where the heating rate $\mathcal{H}_C \propto n_e$ and $u \propto \Delta^0$. Heating from dark matter annihilations (e.g. Mapelli et al. 2006; Cirelli et al. 2009; Liu et al. 2021) would need to be fine-tuned to avoid a substantial injection of energy into the IGM at $z > 2.5$. Cosmic rays can introduce significant non-thermal pressure in the IGM (Lacki 2015; Butsky et al. 2020), but they are not expected to directly increase the temperature of the low density IGM unless they can efficiently couple to the gas (Nath & Biermann 1993; Samui et al. 2018). Further study will be necessary for confirming or ruling out these possibilities, however.

In this work we instead focus on photoelectric emission by dust grains (Nath et al. 1999; Weingartner & Draine 2001; Inoue & Kamaya 2003), by virtue of the fact this heating rate should naturally increase toward lower redshift as the IGM is enriched with heavy elements. Large, high velocity dust grains with sizes $\gtrsim 0.1\mu\text{m}$ and velocities $v \gtrsim 100\text{km s}^{-1}$ may be able to escape into the low density IGM (Bianchi & Ferrara 2005), where the destruction timescale due to thermal sputtering will exceed a Hubble time (Draine 2011). Smaller, slower grains are instead more likely to be eroded within hot halo gas where the sputtering timescale is much shorter. Following Inoue & Kamaya (2010), the specific energy from dust heating scales as $u \propto \Delta^{1/3} T^{-1/6} \propto \Delta^{1/3 - (\gamma - 1)/6}$, where the heating rate is proportional to the dust-to-gas mass ratio, \mathcal{D} , and depends on the uncertain grain size distribution. The density dependence of u also implies that dust heating should flatten the power law temperature-density relation in the low redshift IGM (i.e. $\gamma < 1.6$), in addition to raising the gas temperature. Inoue & Kamaya (2010) provide an approximate expression for the dust heating rate (their eq. 16) assuming the grain size distribution from Mathis et al. (1977). Taking the Puchwein et al. (2019) UV background model and adding the Inoue & Kamaya (2010) heating rate at $z < 2.5$, we find a constant dust-to-gas mass ratio of $\mathcal{D} = 1.5 \times 10^{-3}$ gives an additional $\simeq 6.5\text{eV}$ ($\simeq 4.0\text{eV}$) per proton at $\Delta = 10$ ($\Delta = 1$) by $z = 0.1$. For comparison, $\mathcal{D} \sim 10^{-2}$ for the Milky Way (Draine 2011), while observations of nearby galaxies exhibit a large scatter (2–3 dex) in \mathcal{D} at fixed metallicity (Rémy-Ruyer et al. 2014; De Vis et al. 2019). If we adopt a naive extrapolation of the observed dust-to-gas and metallicity relation from local galaxies (e.g. De Vis et al. 2019) to the $z \sim 0$ IGM, $\mathcal{D} \sim 10^{-3}$ is broadly consistent with $Z \gtrsim 0.1Z_{\odot}$. The requisite heating is therefore only possible if the low density IGM is highly enriched by a viable dust transport mechanism (e.g. galactic winds or radiation pressure). Further investigation of the expected heating rates using a more detailed dust model (e.g. Popping et al. 2017; McKinnon et al. 2017; Hou et al. 2019; Li et al. 2019), along with updated assessment of whether or not dust can be effectively transported into the IGM without being eroded by hot halo gas may be of interest.

Alternatively, if non-canonical heating is negligible, how plausible is our crude upper limit on the (density dependent) line of sight turbulent velocity, $v_{\text{turb}} \lesssim 8.5\text{km s}^{-1} (N_{\text{HI}}/10^{13.5}\text{cm}^{-2})^{0.21}$? Assuming the IGM has kinematic viscosity $\nu \simeq 5 \times 10^{24}\text{cm}^2\text{s}^{-1}$

(Evoli & Ferrara 2011)¹¹, if the typical flow speed in the Ly α forest is the speed of sound, $U = c_s \sim 25\text{km s}^{-1}$, and the characteristic length scale of Ly α forest absorbers at $z \simeq 0.1$ is the Jeans scale, $L \simeq L_{\text{Jeans}} \simeq 250\text{pkpc}$ (Schaye 2001), the Reynolds number for the low redshift Ly α forest is $\text{Re} = UL/\nu \simeq 3.9 \times 10^5$. Although only an order of magnitude estimate, $\text{Re} \gg 10^3$ suggests that, if an appropriate mechanism for continuously generating vorticity is present (e.g. feedback, shocks or magnetic fields), the IGM should indeed be turbulent on small scales (Evoli & Ferrara 2011; Gregori et al. 2012; Iapichino et al. 2013; Zhu et al. 2013). However, given that the Doppler widths of the Ly α absorbers in our simulations decrease with increasing mass resolution (see Appendix A), this implies that – if present – any turbulence must be injected below a spatial resolution scale of roughly $l_{\text{res}} \simeq L_{\text{box}}(N_{\text{part}}/2)^{-1/3}\Delta^{-1/3}$ in the simulations (i.e. $l_{\text{res}} \sim 40\text{ckpc}$ at $\Delta = 10$ for the N1024 simulation). Alternatively, it could be that the gas responsible for the bulk of the low column density Ly α absorption is just not sufficiently agitated by the shocks and/or outflows within our models, or there is some other non-thermal broadening missing in the simulated spectra. Regarding the latter possibility, we note again, however, that most of the Ly α absorbers in our fiducial AGN simulation with $10^{13.3}\text{cm}^{-2} \leq N_{\text{HI}} \leq 10^{14.5}\text{cm}^{-2}$ are already suprathermal with a median $b/b_{\text{therm}} = 1.28$. If adding a turbulent component by hand, such that $b_{\text{turb}} = 0.73b_{\text{noturb}}$, we instead obtain a median $b/b_{\text{therm}} = 1.48$. Both of these values are consistent with the curve-of-growth analysis presented by Danforth et al. (2010), who find $b_{\text{Ly}\alpha}/b_{\text{cog}} = 1.26^{+0.49}_{-0.25}$.

Nevertheless, if taking our turbulent velocity estimate at face value, it is consistent with the results from the galactic outflow driven IGM turbulence model of Evoli & Ferrara (2011) at the higher redshift of $z = 1$, where from their fig. 5, $b_{\text{turb}} = 8 \pm 4\text{km s}^{-1}$ for $N_{\text{HI}} \simeq 10^{13.6}\text{cm}^{-2}$. Observationally, non-thermal broadening can also be constrained by measuring the Doppler parameters of species with different masses in the same gas phase (e.g. Rauch et al. 1996). However, while there is some evidence for turbulence in the low redshift CGM from well aligned O VI, C IV and H I absorbers at $z < 0.5$ (Tripp et al. 2008; Thom & Chen 2008; Savage et al. 2014; Werk et al. 2016; Manuwal et al. 2021), the picture for the lower density diffuse IGM is arguably less clear. The few existing constraints instead come from observations of the Ly α forest at $z \simeq 3$. This has been attempted with H I and He II Ly α absorption, where Zheng et al. (2004) found evidence for purely turbulent broadening from the Doppler parameter ratio of aligned H I and He II Ly α lines. However, in an independent analysis, Fechner & Reimers (2007) found that just under half of aligned He II and H I Ly α absorbers are consistent with purely turbulent broadening. This confusion arises in part because, at $z \simeq 3$, the Hubble broadening of Ly α absorbers across the Jeans smoothing scale, $b_{\text{Jeans}} \simeq H(z)L_{\text{Jeans}}$, becomes comparable to the thermal widths of the lines (e.g. Peebles et al. 2010; Garzilli et al. 2015). Hence, without a self-consistent hydrodynamical model for the IGM density field, this ‘‘Jeans smoothing’’ can easily be confused with turbulence.

Rauch et al. (2001b) side-stepped this problem by measuring *transverse* correlations between the Ly α absorption in gravitationally lensed quasar images separated by $\sim 0.3\text{ckpc}$ at $z \sim 3$. They

¹¹ For comparison, adopting representative values for the temperature and density in the Ly α forest at $z = 0.1$, $T = 10^{4.5}\text{K}$ and $n_{\text{H}} = 10^{-5.5}\text{cm}^{-3}$, the kinematic viscosity of fully ionised hydrogen is $\nu = 2.9 \times 10^{24}\text{cm}^2\text{s}^{-1}$ (Chapman 1954). The suggests $\nu \sim 10^{24}\text{cm}^2\text{s}^{-1}$ provides a reasonable order-of-magnitude estimate for the IGM kinematic viscosity at $z \simeq 0.1$.

found no evidence for turbulence on this scale, although this may not be surprising: the Ly α forest at $z \sim 3$ is sensitive to gas close to the mean density (Becker et al. 2011) and is therefore unlikely to be disturbed by shocks or feedback (Theuns et al. 2002b; Viel et al. 2013; Chabanier et al. 2020). By contrast, in a companion study of CIV absorbers at $z \sim 2-3$ in three lensed quasars (where the typical gas densities probed are more like $\Delta \sim 10-100$, Bolton & Viel (2011)), Rauch et al. (2001a) found that a turbulent velocity component of $v_{\text{turb}} \sim 4.7 \text{ km s}^{-1}$ was required at a scale of $\sim 0.3 \text{ ckpc}$, which is consistent with our (line of sight) estimate of $\lesssim 8.5 \text{ km s}^{-1}$ for $N_{\text{HI}} \sim 10^{13.5} \text{ cm}^{-2}$. At a minimum, this suggests that our crude upper limit on the turbulent contribution to the coldest Ly α forest absorbers at $z = 0.1$ is at least plausible. If a suitably lensed background source could be identified for the Ly α forest at $z < 0.5$, repeating the Rauch et al. (2001b) experiment at $z \simeq 0.1$ would be valuable for testing this possibility further.

6 CONCLUSIONS

We have performed a Voigt profile analysis of the column density distribution function (CDDF) and Doppler parameter distribution measured from hydrodynamical simulations and *Cosmic Origins Spectrograph* (COS) observations of the low redshift Ly α forest at $z \simeq 0.1$ (Viel et al. 2017; Kim et al. 2021). We re-examine the tension between the observations and theoretical predictions for the widths of the Ly α forest absorption lines, where the Ly α absorber Doppler parameters in hydrodynamical simulations are too narrow with respect to the COS data (Nasir et al. 2017; Gaikwad et al. 2017b). We also assess the level of agreement between the COS Ly α forest CDDF and simulations, a statistic that is sensitive to both the UV background amplitude and (sufficiently strong) AGN feedback (Kollmeier et al. 2014; Shull et al. 2015; Khaire & Srianand 2015; Gurvich et al. 2017; Christiansen et al. 2020). Our primary conclusions are as follows.

- We focus on absorption lines with column densities $10^{13.3} \text{ cm}^{-2} \leq N_{\text{HI}} \leq 10^{14.5} \text{ cm}^{-2}$ and Doppler parameters $20 \text{ km s}^{-1} \leq b \leq 90 \text{ km s}^{-1}$ at $z \simeq 0.1$. We show these absorption lines will be minimally impacted by systematic uncertainties in the signal-to-noise and spectral resolution of the data. In this range, the majority of the absorbers (83 per cent) we identify in our fiducial simulation (AGN) reside in the diffuse IGM (i.e. gas with $T < 10^5 \text{ K}$ and $\Delta < 97.2$). Strong absorbers with $N_{\text{HI}} \geq 10^{14} \text{ cm}^{-2}$ are preferentially located close to haloes, with over half of these within $r < 3R_{\text{vir}}$ of haloes of (total) mass $10^{10} M_{\odot} \leq M_{\text{h}} \leq 10^{12} M_{\odot}$ (cf. Chen & Mulchaey 2009; Tejos et al. 2014; Keeney et al. 2018). By contrast, fewer than 10 per cent of $N_{\text{HI}} \geq 10^{14} \text{ cm}^{-2}$ absorbers are within $r < 3R_{\text{vir}}$ of haloes of mass $M_{\text{h}} \geq 10^{12} M_{\odot}$. Hot, collisionally ionised gas from shocks and feedback reduces the incidence of strong absorbers around the most massive haloes at $z = 0.1$.

- After applying a small correction for box size and mass resolution, our fiducial AGN and Quick-Ly α (H02) simulations are both in good agreement (within $\sim 1-1.5\sigma$) with the shape of the CDDF measured from the COS data at $10^{13.3} \text{ cm}^{-2} \leq N_{\text{HI}} \leq 10^{14.5} \text{ cm}^{-2}$. Adopting an H I photoionisation rate, Γ_{HI} , that is ~ 0.6 times the Puchwein et al. (2019) model (or ~ 1.7 times the Haardt & Madau (2012) model) provides a good match to the amplitude of the COS CDDF. We confirm that potent AGN feedback and/or blazar heating models that produce a substantial fraction of the low density, warm-hot IGM (WHIM) further lower the Γ_{HI} required for consistency with the CDDF amplitude (cf. Christiansen et al. 2020), and

will also flatten the CDDF at $N_{\text{HI}} \sim 10^{14} \text{ cm}^{-2}$ (Gurvich et al. 2017).

- The simulated Doppler width distribution for lines with $10^{13.3} \text{ cm}^{-2} \leq N_{\text{HI}} \leq 10^{14.5} \text{ cm}^{-2}$ is inconsistent with the COS measurements; the number of narrow lines with $b = 22.5 \pm 2.5 \text{ km s}^{-1}$ are over-predicted by 4.6σ in our fiducial AGN model. We show that introducing additional hot gas into the low density IGM by invoking strong AGN feedback or blazar heating does not resolve this discrepancy. As already noted by Viel et al. (2017), this is because this hot gas is primarily in the WHIM with temperatures $T \simeq 10^6 \text{ K}$. While this changes the average ionisation level of the IGM (and hence induces a shift the amplitude and shape of the CDDF), it does not produce additional Ly α absorption at the necessary density and temperature for resolving the discrepancy in the line widths. We argue this implies the presence of additional heating or turbulence in the low density IGM.

- We perform a joint analysis of the CDDF and Doppler parameter distribution to find the best fit values for the metagalactic H I photoionisation rate, Γ_{HI} , and the effective power-law spectral index, α_{eff} (where $J_{\text{E}} \propto E^{-\alpha_{\text{eff}}}$), of the UV background close to the Lyman limit. Assuming there is no missing non-thermal broadening in the simulations (e.g., from turbulence), the best fit values are $\log(\Gamma_{\text{HI}}/\text{s}^{-1}) = -13.25_{-0.06}^{+0.03}$ and $\alpha_{\text{eff}} = -0.43_{-0.26}^{+0.13}$ for $\chi^2/\nu = 1.04$. While this photoionisation rate is consistent with previous constraints (Shull et al. 2015; Gaikwad et al. 2017a; Khaire et al. 2019; Caruso et al. 2019), the inferred value of α_{eff} is unphysically hard and is inconsistent by $6-7\sigma$ (statistical) with the much softer spectral shape, $\alpha_{\text{eff}} \simeq -1-1.4$, predicted by state-of-the-art UV background synthesis models that use intrinsic power-law spectral indices of $\alpha_{\text{qso}} = 1.4-2.0$ (Haardt & Madau 2012; Khaire & Srianand 2019; Puchwein et al. 2019; Faucher-Giguère 2020). Even if allowing for a rather extreme UV background with $\alpha_{\text{eff}} \simeq 0$, as might be expected for intrinsic quasar extreme-UV spectral indices of $\alpha_{\text{qso}} = 0.5$ (Scott et al. 2004; Tilton et al. 2016) combined with some spectral hardening by the IGM at the He II ionisation edge, this remains a $\sim 2\sigma$ discrepancy. We conclude that enhanced UV background photoheating rates in the low density IGM that increase the thermally broadened line components are disfavoured as the only solution to the discrepancy between the observed and simulated Ly α forest line widths at $z = 0.1$.

- If taking the UV background heating rates from Puchwein et al. (2019) as a prior (with $\alpha_{\text{eff}} = 1.17$), we may instead appeal to a non-canonical source of heating in the IGM (i.e. heating that is not due to photoheating by the UV background). We then find a specific energy injection of $u \lesssim 6.9 \text{ eV m}_p^{-1}$ in addition to that expected from UV photoheating is required for gas with $\Delta = 10$ at $z < 2.5$. We briefly discuss the likelihood that other physical processes could contribute the additional energy, including heating by dark matter annihilations (Mapelli et al. 2006; Cirelli et al. 2009; Liu et al. 2021), Compton heating by X-rays (Madau & Efstathiou 1999), cosmic rays (Nath & Biermann 1993; Samui et al. 2018) and photoelectric emission by dust grains (Nath et al. 1999; Weingartner & Draine 2001; Inoue & Kamaya 2003). We speculate on the role of dust heating in particular, as the specific energy injected into the IGM scales as $\sim \Delta^{1/3} T^{-1/6}$, and (unlike other mechanisms) the heating rate should naturally increase toward lower redshift as the IGM is enriched with heavy elements. On adopting the dust heating rates from Inoue & Kamaya (2010), an additional $\simeq 6.5 \text{ eV m}_p^{-1}$ at $z < 2.5$ requires a constant dust to gas ratio of $\mathcal{D} = 1.5 \times 10^{-3}$ for

mildly overdense IGM gas with $\Delta = 10$. This is broadly consistent with a metallicity of $Z \gtrsim 0.1Z_{\odot}$, based on a naive extrapolation of the dust-to-gas and metallicity relation in local galaxies, and would therefore imply a highly enriched IGM. However, it remains an open question as to whether or not sufficient quantities of dust can survive passage through hot halo gas (but see [Bianchi & Ferrara 2005](#)). A combination of several non-canonical heating mechanisms along with some non-thermal line broadening may also provide a plausible route for reconciling the COS Ly α line widths and the simulations.

- Alternatively, the additional line broadening may be entirely due to non-thermal broadening that is missing in the hydrodynamical simulations. If again adopting a prior limit on the thermal widths of the Ly α absorbers using the [Puchwein et al. \(2019\)](#) UV background model, we obtain a crude upper limit on a possible additional turbulent contribution to the Ly α forest line widths. For an assumed line width ratio of $b_{\text{turb}}/b_{\text{noturb}} = 0.73$, the best fit UV background parameters are instead $\log(\Gamma_{\text{HI}}/\text{s}^{-1}) = -13.14^{+0.02}_{-0.03}$ and $\alpha_{\text{eff}} = 1.33^{+0.30}_{-0.35}$, where α_{eff} is now consistent with [Puchwein et al. \(2019\)](#) by design. For the coldest gas in the diffuse IGM at $z \simeq 0.1$, the ratio $b_{\text{turb}}/b_{\text{noturb}} = 0.73$ translates to an upper limit of $v_{\text{turb}} \lesssim 8.5 \text{ km s}^{-1} (\text{N}_{\text{HI}}/10^{13.5} \text{ cm}^{-2})^{0.21}$ for the additional turbulent velocity component along the line of sight. This estimate is comparable to theoretical estimates at $z = 1$ ([Evoli & Ferrara 2011](#)) and observational estimates of turbulence from CIV absorbers at $z \sim 3$ ([Rauch et al. 2001a](#)), and would suggest that the stirring of the low density IGM is widespread by $z \simeq 0$.

In summary, we reaffirm that the low redshift Ly α forest provides a powerful diagnostic of complex and poorly understood physical processes in low density *intergalactic* gas. It would be interesting to assess how well numerical models that are anchored to these data reproduce the observed relationship between galaxies and gas at higher densities and on smaller scales at $z < 0.5$.

ACKNOWLEDGEMENTS

We thank the referee, Mike Shull, for a constructive report, and Peng Oh, Sebastiano Cantalupo and George Becker for useful discussions during the early stages of this work, during the ‘‘What matter(s) between galaxies’’ conference held at Abbazia di Spineto in 2019. Our thanks also to Raghunathan Srianand and Sowgat Muzahid for comments on the draft version of the manuscript. The hydrodynamical simulations were performed using the Cambridge Service for Data Driven Discovery (CSD3), part of which is operated by the University of Cambridge Research Computing on behalf of the STFC DiRAC HPC Facility (www.dirac.ac.uk). The DiRAC component of CSD3 was funded by BEIS capital funding via STFC capital grants ST/P002307/1 and ST/R002452/1 and STFC operations grant ST/R00689X/1. This work also used the DiRAC@Durham facility managed by the Institute for Computational Cosmology on behalf of the STFC DiRAC HPC Facility. The equipment was funded by BEIS capital funding via STFC capital grants ST/P002293/1 and ST/R002371/1, Durham University and STFC operations grant ST/R000832/1. DiRAC is part of the National e-Infrastructure. We thank Volker Springel for making P-GADGET-3 available. JSB is supported by STFC consolidated grant ST/T000171/1. For the purpose of open access, the author has applied a creative commons attribution (CC BY) to any author accepted manuscript version arising.

DATA AVAILABILITY

All data and analysis code used in this work are available from the first author on reasonable request.

REFERENCES

- Altay G., Theuns T., Schaye J., Crighton N. H. M., Dalla Vecchia C., 2011, *ApJ*, **737**, L37
- Becker G. D., Bolton J. S., 2013, *MNRAS*, **436**, 1023
- Becker G. D., Bolton J. S., Haehnelt M. G., Sargent W. L. W., 2011, *MNRAS*, **410**, 1096
- Bianchi S., Ferrara A., 2005, *MNRAS*, **358**, 379
- Boera E., Murphy M. T., Becker G. D., Bolton J. S., 2014, *MNRAS*, **441**, 1916
- Bolton J. S., Viel M., 2011, *MNRAS*, **414**, 241
- Bolton J. S., Haehnelt M. G., Viel M., Springel V., 2005, *MNRAS*, **357**, 1178
- Bolton J. S., Oh S. P., Furlanetto S. R., 2009, *MNRAS*, **395**, 736
- Bolton J. S., Puchwein E., Sijacki D., Haehnelt M. G., Kim T.-S., Meiksin A., Regan J. A., Viel M., 2017, *MNRAS*, **464**, 897
- Bryan G. L., Norman M. L., 1998, *ApJ*, **495**, 80
- Butsky I. S., Fielding D. B., Hayward C. C., Hummels C. B., Quinn T. R., Werk J. K., 2020, *ApJ*, **903**, 77
- Carswell R. F., Webb J. K., 2014, VPFIT: Voigt profile fitting program (ascl:1408.015)
- Caruso D., Haardt F., Fumagalli M., Cantalupo S., 2019, *MNRAS*, **482**, 2833
- Chabanier S., Bournaud F., Dubois Y., Palanque-Delabrouille N., Yèche C., Armengaud E., Peirani S., Beckmann R., 2020, *MNRAS*, **495**, 1825
- Chabrier G., 2003, *PASP*, **115**, 763
- Chang P., Broderick A. E., Pfrommer C., 2012, *ApJ*, **752**, 23
- Chapman S., 1954, *ApJ*, **120**, 151
- Chen H.-W., Mulchaey J. S., 2009, *ApJ*, **701**, 1219
- Christiansen J. F., Davé R., Sorini D., Anglés-Alcázar D., 2020, *MNRAS*, **499**, 2617
- Cirelli M., Iocco F., Panci P., 2009, *J. Cosmology Astropart. Phys.*, **2009**, 009
- Danforth C. W., Shull J. M., 2008, *ApJ*, **679**, 194
- Danforth C. W., Stocke J. T., Shull J. M., 2010, *ApJ*, **710**, 613
- Danforth C. W., et al., 2016, *ApJ*, **817**, 111
- Davé R., Hernquist L., Katz N., Weinberg D. H., 1999, *ApJ*, **511**, 521
- Davé R., Oppenheimer B. D., Katz N., Kollmeier J. A., Weinberg D. H., 2010, *MNRAS*, **408**, 2051
- Davé R., Anglés-Alcázar D., Narayanan D., Li Q., Rafieferantsoa M. H., Appleby S., 2019, *MNRAS*, **486**, 2827
- De Vis P., et al., 2019, *A&A*, **623**, A5
- Draine B. T., 2011, *Physics of the Interstellar and Intergalactic Medium*
- Evoli C., Ferrara A., 2011, *MNRAS*, **413**, 2721
- Faucher-Giguère C.-A., 2020, *MNRAS*, **493**, 1614
- Faucher-Giguère C.-A., Lidz A., Zaldarriaga M., Hernquist L., 2009, *ApJ*, **703**, 1416
- Fechner C., Reimers D., 2007, *A&A*, **463**, 69
- Gaikwad P., Khaire V., Choudhury T. R., Srianand R., 2017a, *MNRAS*, **466**, 838
- Gaikwad P., Srianand R., Choudhury T. R., Khaire V., 2017b, *MNRAS*, **467**, 3172
- Gaikwad P., Srianand R., Haehnelt M. G., Choudhury T. R., 2021, *MNRAS*, **506**, 4389
- Garzilli A., Theuns T., Schaye J., 2015, *MNRAS*, **450**, 1465
- Green J. C., et al., 2012, *ApJ*, **744**, 60
- Gregori G., et al., 2012, *Nature*, **481**, 480
- Greig B., Bolton J. S., Wyithe J. S. B., 2015, *MNRAS*, **447**, 2503
- Gurvich A., Burkhardt B., Bird S., 2017, *ApJ*, **835**, 175
- Haardt F., Madau P., 2012, *ApJ*, **746**, 125
- Henden N. A., Puchwein E., Shen S., Sijacki D., 2018, *MNRAS*, **479**, 5385
- Hernquist L., Katz N., Weinberg D. H., Miralda-Escudé J., 1996, *ApJ*, **457**, L51
- Hiss H., Walther M., Hennawi J. F., Oñorbe J., O’Meara J. M., Rorai A., Lukić Z., 2018, *ApJ*, **865**, 42

- Hou K.-C., Aoyama S., Hirashita H., Nagamine K., Shimizu I., 2019, *MNRAS*, **485**, 1727
- Hsyu T., Cooke R. J., Prochaska J. X., Bolte M., 2020, *ApJ*, **896**, 77
- Hui L., Gnedin N. Y., 1997, *MNRAS*, **292**, 27
- Hui L., Haiman Z., 2003, *ApJ*, **596**, 9
- Iapichino L., Viel M., Borgani S., 2013, *MNRAS*, **432**, 2529
- Inoue A. K., Kamaya H., 2003, *MNRAS*, **341**, L7
- Inoue A. K., Kamaya H., 2010, *Earth, Planets, and Space*, **62**, 69
- Keeney B. A., et al., 2018, *ApJS*, **237**, 11
- Khairé V., Srianand R., 2015, *MNRAS*, **451**, L30
- Khairé V., Srianand R., 2019, *MNRAS*, **484**, 4174
- Khairé V., et al., 2019, *MNRAS*, **486**, 769
- Kim T. S., et al., 2021, *MNRAS*, **501**, 5811
- Kollmeier J. A., et al., 2014, *ApJ*, **789**, L32
- Kulkarni G., Worseck G., Hennawi J. F., 2019, *MNRAS*, **488**, 1035
- Lacki B. C., 2015, *MNRAS*, **448**, L20
- Li Q., Narayanan D., Davé R., 2019, *MNRAS*, **490**, 1425
- Lidz A., Heitmann K., Hui L., Habib S., Rauch M., Sargent W. L. W., 2006, *ApJ*, **638**, 27
- Liu H., Qin W., Ridgway G. W., Slatyer T. R., 2021, *Phys. Rev. D*, **104**, 043514
- Lukić Z., Stark C. W., Nugent P., White M., Meiksin A. A., Almgren A., 2015, *MNRAS*, **446**, 3697
- Lusso E., Worseck G., Hennawi J. F., Prochaska J. X., Vignali C., Stern J., O’Meara J. M., 2015, *MNRAS*, **449**, 4204
- Madau P., Efstathiou G., 1999, *ApJ*, **517**, L9
- Maitra S., Srianand R., Gaikwad P., 2022, *MNRAS*, **509**, 1536
- Manuwal A., Narayanan A., Udhwani P., Srianand R., Savage B. D., Charlton J. C., Misawa T., 2021, *MNRAS*, **505**, 3635
- Mapelli M., Ferrara A., Pierpaoli E., 2006, *MNRAS*, **369**, 1719
- Marinacci F., et al., 2018, *MNRAS*, **480**, 5113
- Mathis J. S., Ruml W., Nordsieck K. H., 1977, *ApJ*, **217**, 425
- McKinnon R., Torrey P., Vogelsberger M., Hayward C. C., Marinacci F., 2017, *MNRAS*, **468**, 1505
- McQuinn M., 2016, *ARA&A*, **54**, 313
- McQuinn M., Upton Sanderbeck P. R., 2016, *MNRAS*, **456**, 47
- Miralda-Escudé J., Rees M. J., 1994, *MNRAS*, **266**, 343
- Molaro M., et al., 2022, *MNRAS*, **509**, 6119
- Naiman J. P., et al., 2018, *MNRAS*, **477**, 1206
- Nasir F., Bolton J. S., Becker G. D., 2016, *MNRAS*, **463**, 2335
- Nasir F., Bolton J. S., Viel M., Kim T.-S., Haehnelt M. G., Puchwein E., Sijacki D., 2017, *MNRAS*, **471**, 1056
- Nath B. B., Biermann P. L., 1993, *MNRAS*, **265**, 241
- Nath B. B., Sethi S. K., Shchekinov Y., 1999, *MNRAS*, **303**, 1
- Nelson D., et al., 2018, *MNRAS*, **475**, 624
- Nelson D., et al., 2019, *Computational Astrophysics and Cosmology*, **6**, 2
- Oppenheimer B. D., Davé R., 2009, *MNRAS*, **395**, 1875
- Peeples M. S., Weinberg D. H., Davé R., Fardal M. A., Katz N., 2010, *MNRAS*, **404**, 1281
- Pillepich A., et al., 2018, *MNRAS*, **475**, 648
- Planck Collaboration et al., 2014, *A&A*, **571**, A16
- Popping G., Somerville R. S., Galametz M., 2017, *MNRAS*, **471**, 3152
- Puchwein E., Springel V., 2013, *MNRAS*, **428**, 2966
- Puchwein E., Pfrommer C., Springel V., Broderick A. E., Chang P., 2012, *MNRAS*, **423**, 149
- Puchwein E., Bolton J. S., Haehnelt M. G., Madau P., Becker G. D., Haardt F., 2015, *MNRAS*, **450**, 4081
- Puchwein E., Haardt F., Haehnelt M. G., Madau P., 2019, *MNRAS*, **485**, 47
- Rahmati A., Pawlik A. H., Raicevic M., Schaye J., 2013, *MNRAS*, **430**, 2427
- Rauch M., Sargent W. L. W., Womble D. S., Barlow T. A., 1996, *ApJ*, **467**, L5
- Rauch M., Sargent W. L. W., Barlow T. A., 2001a, *ApJ*, **554**, 823
- Rauch M., Sargent W. L. W., Barlow T. A., Carswell R. F., 2001b, *ApJ*, **562**, 76
- Rémy-Ruyer A., et al., 2014, *A&A*, **563**, A31
- Ricotti M., Gnedin N. Y., Shull J. M., 2000, *ApJ*, **534**, 41
- Rorai A., et al., 2017, *MNRAS*, **466**, 2690
- Rossi G., 2020, *ApJS*, **249**, 19
- Salpeter E. E., 1955, *ApJ*, **121**, 161
- Samui S., Subramanian K., Srianand R., 2018, *MNRAS*, **476**, 1680
- Savage B. D., Kim T. S., Wakker B. P., Keeney B., Shull J. M., Stocke J. T., Green J. C., 2014, *ApJS*, **212**, 8
- Schaye J., 2001, *ApJ*, **559**, 507
- Schaye J., Theuns T., Rauch M., Efstathiou G., Sargent W. L. W., 2000, *MNRAS*, **318**, 817
- Scott J. E., Kriss G. A., Brotherton M., Green R. F., Hutchings J., Shull J. M., Zheng W., 2004, *ApJ*, **615**, 135
- Shen X., Hopkins P. F., Faucher-Giguère C.-A., Alexander D. M., Richards G. T., Ross N. P., Hickox R. C., 2020, *MNRAS*, **495**, 3252
- Shull J. M., Danforth C. W., 2020, *ApJ*, **899**, 163
- Shull J. M., et al., 2000, *ApJ*, **538**, L13
- Shull J. M., Moloney J., Danforth C. W., Tilton E. M., 2015, *ApJ*, **811**, 3
- Šoltinský T., et al., 2021, *MNRAS*, **506**, 5818
- Springel V., 2005, *MNRAS*, **364**, 1105
- Springel V., 2010, *MNRAS*, **401**, 791
- Springel V., Hernquist L., 2003, *MNRAS*, **339**, 289
- Springel V., et al., 2018, *MNRAS*, **475**, 676
- Stevens M. L., Shull J. M., Danforth C. W., Tilton E. M., 2014, *ApJ*, **794**, 75
- Tejos N., et al., 2014, *MNRAS*, **437**, 2017
- Tepper-García T., 2006, *MNRAS*, **369**, 2025
- Tepper-García T., Richter P., Schaye J., Booth C. M., Dalla Vecchia C., Theuns T., 2012, *MNRAS*, **425**, 1640
- Theuns T., Leonard A., Efstathiou G., 1998a, *MNRAS*, **297**, L49
- Theuns T., Leonard A., Efstathiou G., Pearce F. R., Thomas P. A., 1998b, *MNRAS*, **301**, 478
- Theuns T., Schaye J., Zaroubi S., Kim T.-S., Tzanavaris P., Carswell B., 2002a, *ApJ*, **567**, L103
- Theuns T., Viel M., Kay S., Schaye J., Carswell R. F., Tzanavaris P., 2002b, *ApJ*, **578**, L5
- Thom C., Chen H.-W., 2008, *ApJS*, **179**, 37
- Tilton E. M., Stevens M. L., Shull J. M., Danforth C. W., 2016, *ApJ*, **817**, 56
- Tonnesen S., Smith B. D., Kollmeier J. A., Cen R., 2017, *ApJ*, **845**, 47
- Tripp T. M., Sembach K. R., Bowen D. V., Savage B. D., Jenkins E. B., Lehner N., Richter P., 2008, *ApJS*, **177**, 39
- Upton Sanderbeck P., Bird S., 2020, *MNRAS*, **496**, 4372
- Upton Sanderbeck P. R., D’Aloisio A., McQuinn M. J., 2016, *MNRAS*, **460**, 1885
- Verner D. A., Ferland G. J., 1996, *ApJS*, **103**, 467
- Viel M., Haehnelt M. G., Springel V., 2004, *MNRAS*, **354**, 684
- Viel M., Schaye J., Booth C. M., 2013, *MNRAS*, **429**, 1734
- Viel M., Haehnelt M. G., Bolton J. S., Kim T.-S., Puchwein E., Nasir F., Wakker B. P., 2017, *MNRAS*, **467**, L86
- Villasenor B., Robertson B., Madau P., Schneider E., 2021, *ApJ*, **912**, 138
- Wakker B. P., Hernandez A. K., French D. M., Kim T.-S., Oppenheimer B. D., Savage B. D., 2015, *ApJ*, **814**, 40
- Walther M., Oñorbe J., Hennawi J. F., Lukić Z., 2019, *ApJ*, **872**, 13
- Weingartner J. C., Draine B. T., 2001, *ApJS*, **134**, 263
- Werk J. K., et al., 2016, *ApJ*, **833**, 54
- Wilde M. C., et al., 2021, *ApJ*, **912**, 9
- Worseck G., Davies F. B., Hennawi J. F., Prochaska J. X., 2019, *ApJ*, **875**, 111
- Yang J., et al., 2020, *ApJ*, **904**, 26
- Zheng W., et al., 2004, *ApJ*, **605**, 631
- Zhu W., Feng L.-l., Xia Y., Shu C.-W., Gu Q., Fang L.-Z., 2013, *ApJ*, **777**, 48

APPENDIX A: BOX SIZE AND MASS RESOLUTION

Numerical convergence tests of the Ly α forest CDDF and Doppler parameter distribution with simulation box size and gas particle mass are presented in Fig. A1 and Fig. A2, respectively. The Doppler parameter distribution is well converged with respect to the 1σ uncertainties on the COS data for our fiducial values of

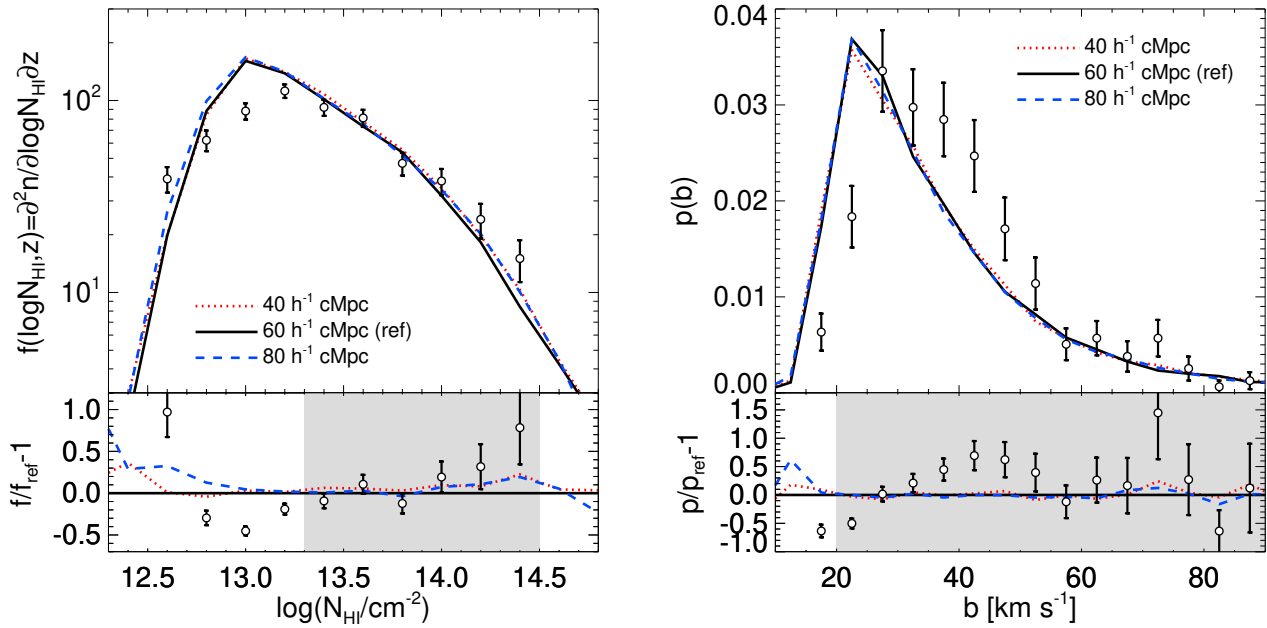


Figure A1. The effect of box size for a fixed gas particle mass. *Left:* The CDDF measured from COS data for Ly α absorbers with Doppler parameters $20 \text{ km s}^{-1} \leq b \leq 90 \text{ km s}^{-1}$, compared to the CDDF obtained from the L40 (red dotted), H02 (black solid) and L80 (blue dashed) simulations. The figure is otherwise the same as Figure 3, but excludes the box size and mass resolution correction to the simulated CDDF. *Right:* The corresponding Doppler parameter probability distribution for Ly α absorbers with column densities $10^{13.3} \text{ cm}^{-2} \leq N_{\text{HI}} \leq 10^{14.5} \text{ cm}^{-2}$.

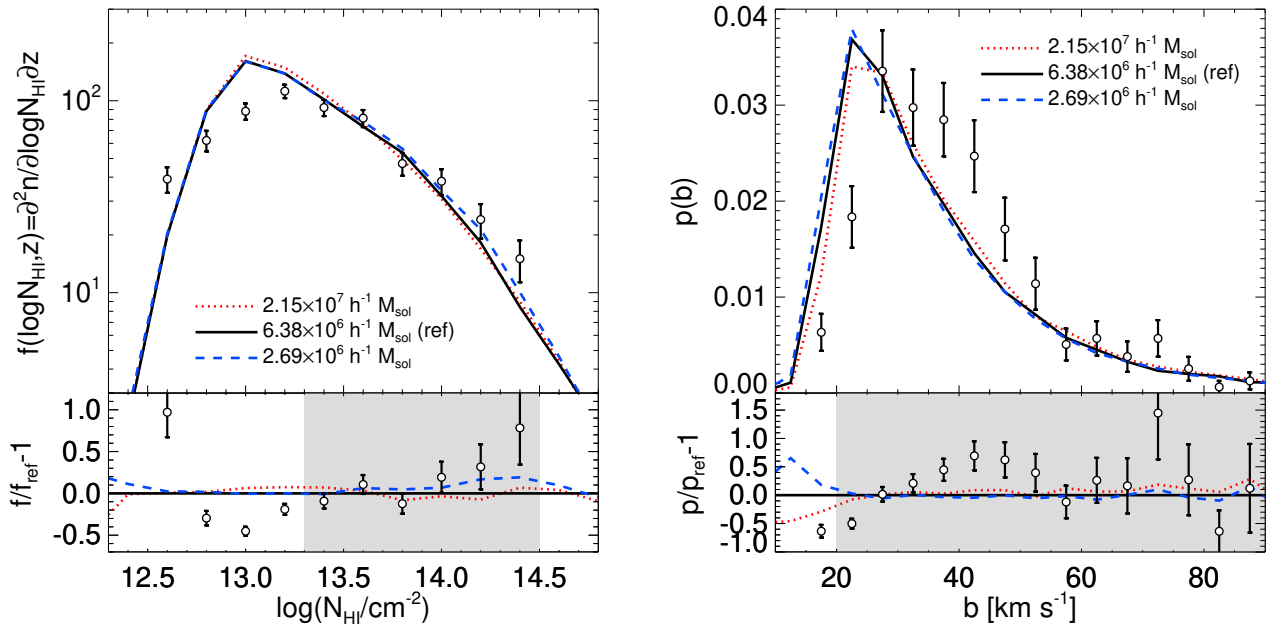


Figure A2. The effect of gas particle mass for fixed box size. *Left:* The CDDF measured from COS data for Ly α absorbers with Doppler parameters $20 \text{ km s}^{-1} \leq b \leq 90 \text{ km s}^{-1}$, compared to the CDDF obtained from the N512 (red dotted), H02 (black solid) and N1024 (blue dashed) simulations. *Right:* The corresponding Doppler parameter probability distribution for Ly α absorbers with column densities $10^{13.3} \text{ cm}^{-2} \leq N_{\text{HI}} \leq 10^{14.5} \text{ cm}^{-2}$. The figure is otherwise the same as Figure 3.

$L = 60 h^{-1} \text{ cMpc}$ and $M_{\text{gas}} = 6.38 \times 10^6 h^{-1} M_{\odot}$. However, a ~ 10 – 30 per cent correction to the CDDF – particularly for strong Ly α absorbers with $N_{\text{HI}} \geq 10^{14} \text{ cm}^{-2}$ – is required on comparing our fiducial model to simulations with $L = 80 h^{-1} \text{ cMpc}$ or $M_{\text{gas}} = 2.69 \times 10^6 h^{-1} M_{\odot}$ (the blue dashed curves in Fig. A1 and Fig. A2). This correction is typically comparable to the 1σ uncertainties on the

COS CDDF measurement. The combined correction for box size and mass resolution that we apply to the CDDF is given in Table A1.

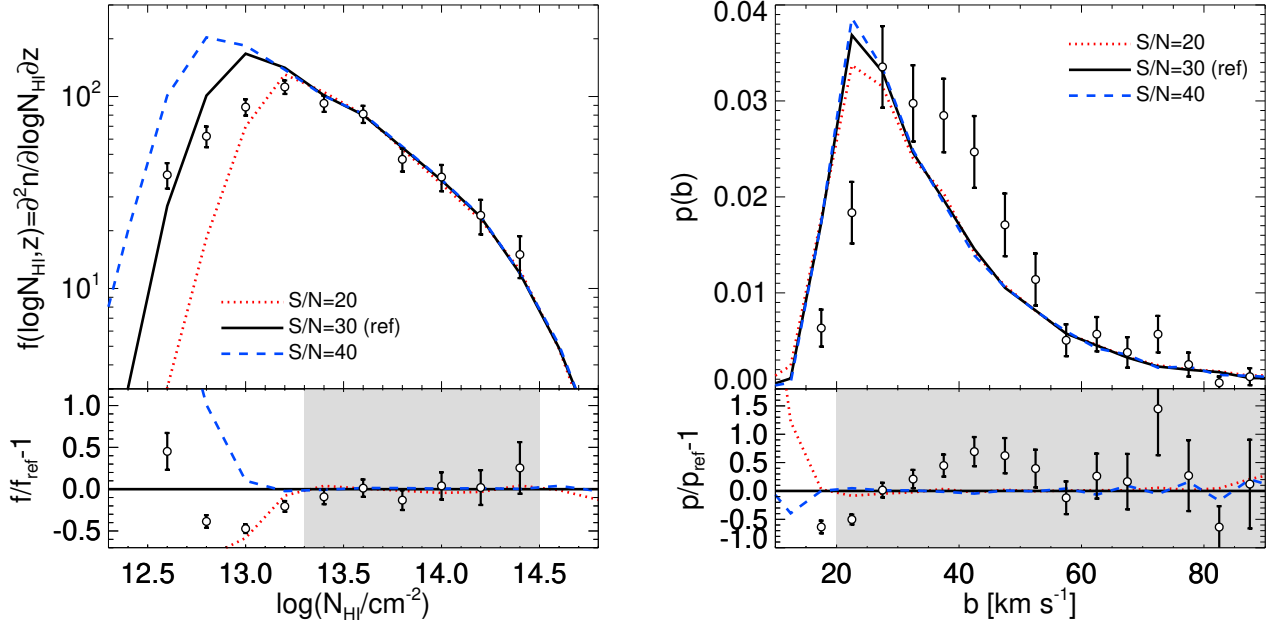


Figure B1. The effect of the signal-to-noise per resolution element. *Left:* The CDDF measured from COS data for Ly α absorbers with Doppler parameters $20\text{km s}^{-1} \leq b \leq 90\text{km s}^{-1}$, compared to the CDDF obtained from the H0 simulation for mock spectra with a flux independent signal-to-noise per resolution element of $S/N = 20$ (red dotted), $S/N = 30$ (black solid) and $S/N = 40$ (blue dashed). *Right:* The corresponding Doppler parameter probability distribution for Ly α absorbers with column densities $10^{13.3}\text{ cm}^{-2} \leq N_{\text{HI}} \leq 10^{14.5}\text{ cm}^{-2}$.

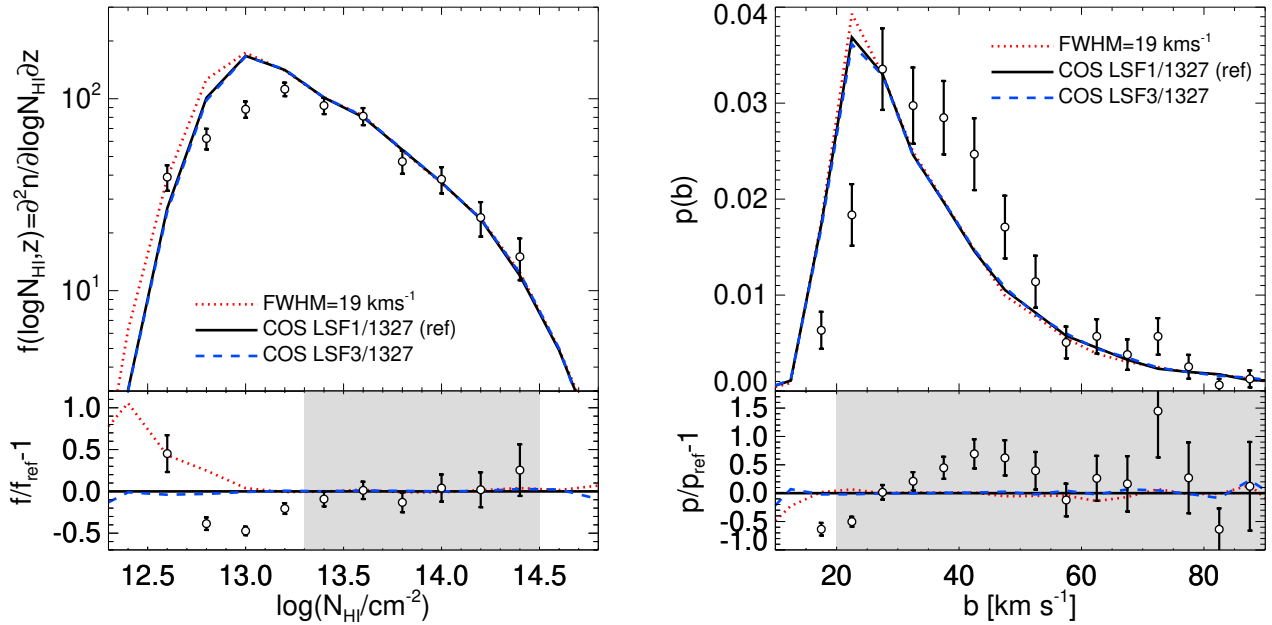


Figure B2. The effect of the COS line spread function. *Left:* The CDDF measured from COS data for Ly α absorbers with Doppler parameters $20\text{km s}^{-1} \leq b \leq 90\text{km s}^{-1}$, compared to the CDDF obtained from the H02 simulation after convolving the mock spectra with a Gaussian line profile with $\text{FWHM} = 19\text{km s}^{-1}$ (red dotted), the COS LSF for central wavelength G130M/1327 at LP1 (black solid) and at LP3 (blue dashed). *Right:* The corresponding Doppler parameter probability distribution for Ly α absorbers with column densities $10^{13.3}\text{ cm}^{-2} \leq N_{\text{HI}} \leq 10^{14.5}\text{ cm}^{-2}$. The figure is otherwise the same as Figure 3.

APPENDIX B: SYSTEMATICS

The effect of the assumed signal-to-noise ratio and line spread function (LSF) on our Voigt profile fits to simulated spectra are shown in Fig. B1 and Fig. B2, respectively.

Our fiducial, flux independent signal-to-noise ratio of $S/N = 30$

per 19km s^{-1} resolution element (black curves) is compared to $S/N = 20$ (red dotted curves) and $S/N = 40$ (blue dashed curves) in Fig. B1. The signal-to-noise ratio affects the identification of narrow ($b < 10\text{km s}^{-1}$) absorbers, and impacts on the completeness of low column density ($N_{\text{HI}} < 10^{13}\text{ cm}^{-2}$) absorption lines. We have also tested more complicated noise models that use a combina-

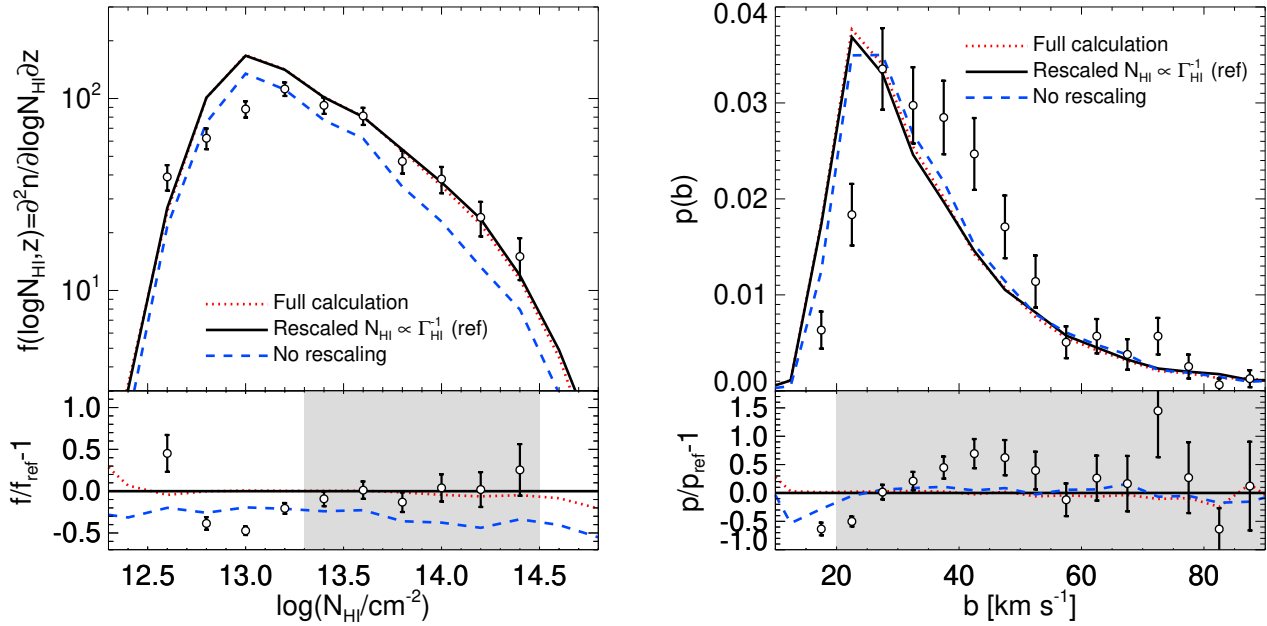


Figure B3. The effect of rescaling the Ly α optical depths under the assumption of photoionisation equilibrium. *Left:* The CDDF measured from COS data for Ly α absorbers with Doppler parameters $20 \text{ km s}^{-1} \leq b \leq 90 \text{ km s}^{-1}$, compared to the CDDF obtained from the H02 simulation for no rescaling (i.e. using the native UV background amplitude, red dotted), a linear rescaling of the pixel optical depths (or equivalently, column densities) in post-processing (black solid) and a full recalculation of the ionisation balance including the effect of collisional ionisation and free electrons from ionised helium (red dotted). *Right:* The corresponding Doppler parameter probability distribution for Ly α absorbers with column densities $10^{13.3} \text{ cm}^{-2} \leq N_{\text{HI}} \leq 10^{14.5} \text{ cm}^{-2}$. The figure is otherwise the same as Figure 3.

Table A1. The correction we apply to each CDDF bin of width $\Delta \log N_{\text{HI}} = 0.2$ to account for the convergence with simulation box size and mass resolution at our fiducial box size and mass resolution of $L = 60 h^{-1} \text{ cMpc}$ and $M_{\text{gas}} = 6.38 \times 10^6 h^{-1} M_{\odot}$. The corrected CDDF is given by $\kappa_{\text{boxres}} f(\log N_{\text{HI}}, z)$.

$\log(N_{\text{HI}}/\text{cm}^{-2})$	κ_{boxres}
13.4	1.00
13.6	1.09
13.8	1.01
14.0	1.15
14.2	1.29
14.4	1.42

tion of flux independent and flux dependent terms (not shown), but we find very little difference between these and a flux independent noise model for lines with $10^{13.3} \text{ cm}^{-2} \leq N_{\text{HI}} \leq 10^{14.5} \text{ cm}^{-2}$ and $20 \text{ km s}^{-1} \leq b \leq 90 \text{ km s}^{-1}$.

In Fig. B2, we show the effect of deconvolving the mock spectra with the COS LSF (G130M/1327 LP1, black curves)¹², as well as the COS LSF at a different lifetime position, G130M/1327 LP3 (blue dashed curves) and a Gaussian with FWHM= 19 km s^{-1} . As was the case for the signal-to-noise, the narrow, low column density lines are the most strongly affected if using an incorrect model for the LSF. This is most apparent for the Gaussian LSF, which lacks the extended wings that are present in the COS LSF.

Based on the results shown in Fig. B1 and Fig. B2, we judge that

¹² <https://www.stsci.edu/hst/instrumentation/cos/performance/spectral-resolution>

Ly α forest absorption lines with $10^{13.3} \text{ cm}^{-2} \leq N_{\text{HI}} \leq 10^{14.5} \text{ cm}^{-2}$ and $20 \text{ km s}^{-1} \leq b \leq 90 \text{ km s}^{-1}$ should be the least affected by variations in the assumed signal-to-noise or spectral resolution of the COS data.

Finally, as discussed in Section 3.2, the HI column densities in our simulated spectra are rescaled by a constant to match the amplitude of the observed CDDF at $10^{13.3} \text{ cm}^{-2} \leq N_{\text{HI}} \leq 10^{14.5} \text{ cm}^{-2}$ (following Viel et al. 2017). This is equivalent to rescaling the HI photoionisation rate, Γ_{HI} , since $N_{\text{HI}} \propto \Gamma_{\text{HI}}^{-1}$ for optically thin gas in photoionisation equilibrium with the UV background. However, as noted by Khaire et al. (2019), it is possible this assumption may break down if the gas responsible for the Ly α forest absorption at $z \simeq 0.1$ is hot ($T > 10^5 \text{ K}$) and collisionally ionised. We test this explicitly in Fig. B3 using three cases: no rescaling of the column densities (blue dashed curves), the post-processed linear scaling of the column densities that we use throughout this work (black curves), and a full recalculation of the IGM ionisation balance using a photoionisation rate that is scaled by the same factor used in the post-processed case (red dotted curves). For the column density and Doppler parameter range we consider in this work, the agreement between the approximate (black curves) and full calculation (red dotted curves) is excellent, justifying our assumption.

APPENDIX C: COMPARISON TO ILLUSTRIS-TNG

In Figure C1, we compare the COS CDDF and Doppler parameter distribution to Voigt profile fits obtained from Ly α forest spectra extracted from the publicly available Illustris TNG100-1 simulation at $z = 0.1$ (Marinacci et al. 2018; Naiman et al. 2018; Nelson et al. 2018; Springel et al. 2018; Pillepich et al. 2018; Nelson et al. 2019).

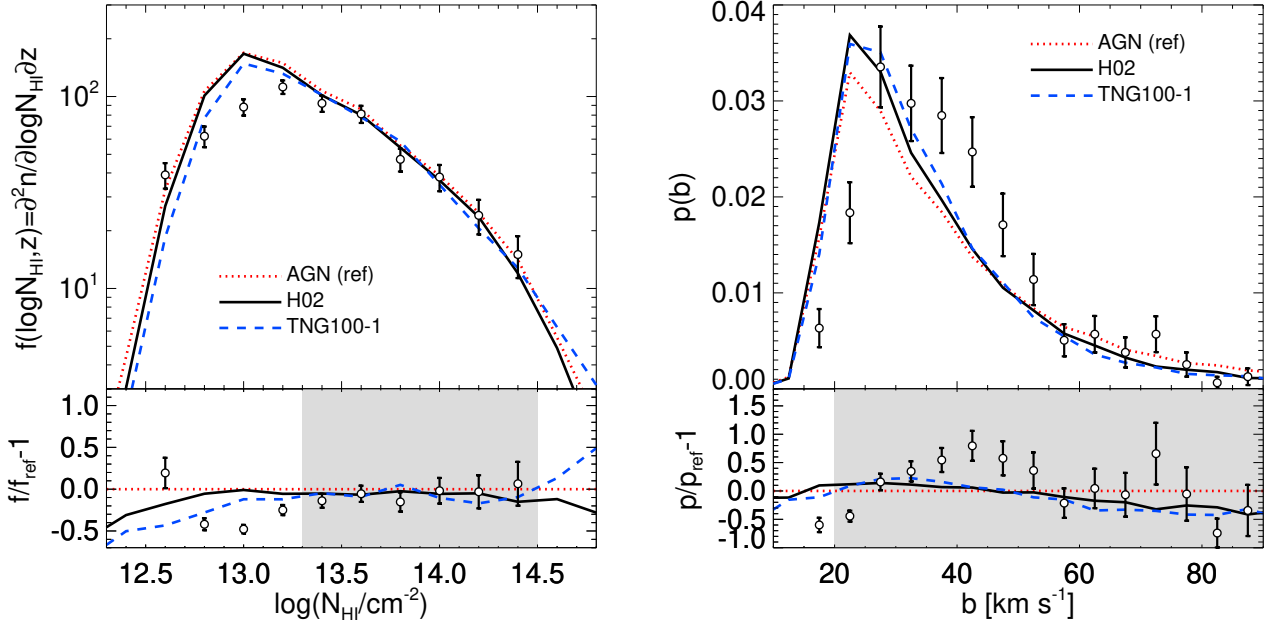


Figure C1. Comparison of the TNG100-1 simulation to the CDDF and Doppler parameter distribution measured from COS data. *Left:* The CDDF for Ly α absorbers with Doppler parameters $20 \text{ km s}^{-1} \leq b \leq 90 \text{ km s}^{-1}$, compared to the TNG100-1 simulation (blue dashed curve), AGN simulation (red dotted curve) and H02 simulation (solid black curve). Note that we do not apply a correction for mass resolution and box size to the CDDF from TNG100-1. *Right:* The corresponding Doppler parameter probability distribution for Ly α absorbers with column densities $10^{13.3} \text{ cm}^{-2} \leq N_{\text{HI}} \leq 10^{14.5} \text{ cm}^{-2}$. The figure is otherwise the same as Figure 3.

This provides a test of whether or not the results of this study are peculiar to our numerical implementation.

In contrast to the simulations used in this work, IllustrisTNG includes metal line cooling and magneto-hydrodynamics, as well as different implementations for AGN feedback, galactic winds, metal enrichment and the UV background. IllustrisTNG furthermore uses the AREPO code (Springel 2010), which employs a moving-mesh hydrodynamics scheme instead of smoothed particle hydrodynamics. The cosmological parameters for the TNG100-1 simulation are very similar to those used in this work, with $\Omega_m = 0.3089$, $\Omega_\Lambda = 0.6911$, $h = 0.6774$, $\Omega_b = 0.0486$, $\sigma_8 = 0.8159$ and $n = 0.9667$. The box size of TNG100-1 is $75 h^{-1} \text{ cMpc}$, with a gas particle mass of $M_{\text{gas}} = 9.4 \times 10^5 h^{-1} M_\odot$ (i.e. a factor ~ 2 larger volume and a factor ~ 7 smaller gas particle mass compared to our fiducial AGN simulation). Photoionisation and photoheating is provided by the 2011 update of the Faucher-Giguère et al. (2009) UV background model.¹³ At $z = 0.1$, this has $\log(\Gamma_{\text{HI}}^{\text{FG09}} / \text{s}^{-1}) = -13.31$.

Adopting $\log(\Gamma_{\text{HI}}^{\text{CDDF}} / \text{s}^{-1}) = -13.08$ in the TNG100-1 Ly α forest spectra provides a good match (within $1-2\sigma$) to the amplitude and shape of the CDDF (this corresponds to $\Gamma_{\text{HI}}^{\text{CDDF}} / \Gamma_{\text{HI}}^{\text{HM12}} = 2.37$). However, the line widths remain systematically narrower than the COS data, with the number of lines at $b = 22.5 \pm 2.5 \text{ km s}^{-1}$ over-predicted by $\sim 5.5\sigma$. This is consistent with the simulations used in this work.

This paper has been typeset from a \LaTeX file prepared by the author.

¹³ <https://galaxies.northwestern.edu/uvb-fg09/>